1 **Resolution of MoS$_2$ nanosheets-induced pulmonary inflammation driven by nanoscale**

2 **intracellular transformation and extracellular-vesicle shuttles**

3

4 *Nathaly Ortiz Peña, Kondareddy Cherukula, Benjamin Even, Ding-Kun Ji, Sarah*

5 *Razafindrakoto, Shiyuan Peng, Amanda K. A. Silva, Cécilia Ménard Moyon, Hervé*

6 *Hillaireau, Alberto Bianco,* Elias Fattal,* Damien Alloyeau,* Florence Gazeau**

7

8 N. Ortiz Peña, D. Alloyeau

9 Université Paris Cité, MPQ Matériaux et Phénomènes Quantiques, CNRS, 10 rue Alice

10 Domon et Léonie Duquet, Paris 75205 Cedex 13, France

11 E-Mail: damien.alloyeau@u-paris.fr

12 K. Cherukula, S. Razafindrakoto, A. K. A. Silva, F. Gazeau

13 E-Mail: florence.gazeau@u-paris.fr

14 Université Paris Cité, MSC Matière et Systèmes Complexes, CNRS, 45 rue des Saints Pères,

15 Paris 75006 France

16 B. Even, H. Hillaireau, E. Fattal

17 E-Mail: elias.fattal@universite-paris-saclay.fr

18 Université Paris-Saclay, CNRS, Institut Galien Paris-Saclay, 91400 Orsay, France

19 D.-K. Ji, S. Peng, C. Ménard Moyon, A. Bianco

20 E-Mail: a.bianco@ibmc-cnrs.unistra.fr

21 CNRS, Immunology, Immunopathology and Therapeutic Chemistry, UPR 3572, University

22 of Strasbourg, ISIS, 67000 Strasbourg, France

23

24

27

28 Pulmonary exposure to some engineered nanomaterials can cause chronic lesions as a result

29 of unresolved inflammation. Among two-dimensional (2D) nanomaterials and graphene,

30 MoS$_2$ have received tremendous attention in optoelectronics and nanomedicine. Here we

31 propose an integrated approach to follow up the transformation of MoS$_2$ nanosheets at the

32 nanoscale and their impact on the lung inflammation status over one month after a single

33 inhalation in mice. Analysis of immune cells, alveolar macrophages, extracellular vesicles,

34 and cytokine profiling in bronchoalveolar lavage fluid (BALF) showed that MoS$_2$ nanosheets

1 induced initiation of lung inflammation that was rapidly resolved despite the persistence of

2 various biotransformed molybdenum-containing nanostructures in alveolar macrophages and

3 extracellular vesicles up to one month. Using *in situ* liquid phase transmission electron

4 microscopy experiments, we could evidence the dynamics of MoS_2 nanosheets transformation

5 triggered by reactive oxygen species. Three main transformation mechanisms were observed

6 directly at the nanoscale level: 1) scrolling of the dispersed sheets leading to the formation of

7 nanoscrolls and folded patches, 2) etching releasing soluble MoO_4^-, and 3) oxidation

8 generating oxidized sheet fragments. Extracellular vesicles released in BALF were also

9 identified as a potential shuttle of MoS_2 nanostructures and their degradation products and

10 more importantly as mediators of inflammation resolution.

11

12 **1. Introduction**

13 Inorganic two-dimensional (2D) materials particularly transition metal dichalcogenides

14 (TMDs) have raised significant attention due to their exceptional electronic, optical,

15 mechanical, and chemical properties.[1,2] Notably, the large surface area with tunable

16 electronic properties, the intercalable layers and bio- functionalization holds great promise in

17 biosensing,[3-5] bioimaging,[6,7] and drug delivery,[8-10] among others applications.[11] In

18 particular, molybdenum disulfide, a graphene analogue consisting of S-Mo-S covalent

19 arrangements[12] is one of the commercially attractive materials used as catalyst, lubricant,

20 welding, and combustion.[2] Furthermore, MoS_2 nanosheets have shown to have better

21 biocompatibility and stability in comparison with their carbon-based analogues,[13,14] and

22 other TMD materials,[15] as well as degradation capacity in an aqueous environment.[16] Prior

23 studies evaluated the adverse effects of MoS_2 *in vitro*[17] or *in vivo*[18] highlighting the MoS_2

24 biotransformation into the oxidized form, like molybdenum oxide (MoO_4^-), and the

25 incorporation of molybdenum into molybdenum enzymes, affecting liver metabolism.[18-21]

26 Heavy metals and particularly molybdenum exposure has been related to health hazards such

27 as fetal growth disturbance,[22] systemic sclerosis,[23] or chronic kidney disease.[24] Depending

28 on the form of TMD and the exfoliation degrees, *in vitro* studies demonstrated different levels

29 of cytotoxicity.[25,26] Additionally, differences in the antibacterial activity were observed

30 between exfoliated MoS_2 and annealed MoS_2 in combination with ethylenediaminetetraacetic

31 acid (EDTA) as an electron donor. The exfoliated MoS_2 form was demonstrated to have a

32 better performance in the inactivation of *Escherichia coli* biofilm production, this difference

33 being attributed to an enhanced creation of reactive oxygen species (ROS) due to their higher

34 electron conductivity when in 2D form.[27]

1   There are several factors affecting the toxicity and degradation capacity of 2D materials

2   including layered structures, degree of exfoliation, surface area, active edge sites etc.

3   However, the mechanisms involved in cell processing of 2D materials and restoration of

4   homeostasis after an inflammatory insult remain little understood. In the context of tissue

5   injury induced by exposure to xenobiotics or nanoparticles, mechanisms of inflammation self-

6   resolution can be deployed to avoid chronic inflammation. This is particularly important in a

7   dynamic immune environment such as the lung, as continuous induction of inflammatory

8   signals could produce irreversible damage to the organs. It is found that foreign agents,

9   damaged/aggregated proteins, misfolded proteins as well as nanoparticles are diverted by cell

10 either to lysosomes that present a harsh acidic and oxidizing environment favorable for

11 transformation and degradation of nanoparticle[39] and/or exocytosed in the extracellular

12 medium with the release of extracellular vesicles (EVs).[29-33] Inorganic nanostructures such as

13 gold nanoparticles or carbon nanotubes can undergo massive degradation and restructuration

14 in lysosomes mediated by ROS.[34,35] However, such intracellular transformation of MoS_2

15 nanosheets has not been investigated in detail and over a long period after exposure *in vivo*.

16 Furthermore, EVs can also spread nanoparticles and aggregated proteins, contributing, for

17 instance, to the progression of neurodegenerative diseases with the active propagation of

18 amyloid peptide and tau protein[33] or disseminating carbon nanotubes or iron oxide

19 nanoparticles to naive cells.[29,31,36] EVs released by cells under different conditions, including

20 nanoparticle exposure produce a multitude of effects such as pro-inflammatory, anti-

21 inflammatory, antigen presentation or cancer growth signals. For example, EVs play a role in

22 shuttling RNA to influence the recipient cell response to external stress.[37] Under

23 pathophysiological conditions, EVs can also transfer defense machinery from one cell to

24 another such as antioxidant molecules enriching the cellular defense mechanisms against

25 specific stress.[38]

26 In this context, we have first investigated whether MoS_2 nanosheets instilled into the trachea

27 of mice could pose a potential hazard to the lung environment and how it can be related to the

28 fate and biotransformations of these nanomaterials in the bronchoalveolar fluid over one

29 month. Transient oxidative stress and a pro-inflammation environment was observed upon

30 MoS_2 lung installation, which was rapidly resolved despite the persistence of intracellular Mo

31 nanostructures in different forms within alveolar macrophages. We thus investigated the

32 mechanisms of nanotransformation of MoS_2 patches both in primary macrophages and in

33 intracellular biomimetic media using *in situ* liquid phase transmission electron microscopy.

34 Secondly, we studied the EVs released in BALF and investigated their role in the resolution

1   of nanoparticle-induced inflammation. Overall, our multiscale investigation provides insight

2   into the dynamic of the cellular transformations of exfoliated MoS_2 nanosheets at the

3   nanoscale in the lung environment and sheds light on their role in resolving the initial

4   inflammation insult related to MoS_2 nanosheet exposure.

5

6   **2. Results and Discussion**

7   2D MoS_2 nanosheets were prepared through liquid phase exfoliation of bulk MoS_2 crystals in

8   an aqueous solution of bile salts. TEM showed MoS_2 nanosheets with a narrow lateral size

9   ranging from 50 to 150 nm (**Figure 1a, Figure S1a**). The HRTEM images suggested the

10   formation of thin layer MoS_2, illustrating the hexagonal symmetry of the material (**Figure**

11   **S1b**). The resulting 2D MoS_2 nanosheets own superior dispersibility in aqueous solution.

12   Colloidal stability was confirmed by the low value of ζ-potential, corresponding to – 38.1

13   mV. The UV-Vis and Raman spectra also confirmed the successful preparation of 2D MoS_2

14   nanosheets (**Figure S2**).[39] The chemical composition of 2D MoS_2 was investigated by X-ray

15   photoelectron spectroscopy (XPS). The two strong peaks in the high resolution spectrum,

16   located at 229.3 and 232.5 eV, correspond to Mo $3d_{5/2}$ and Mo $3d_{3/2}$, respectively. XPS also

17   confirmed that the Mo element was mainly present as Mo (IV) in MoS_2 (**Figure S3**). The

18   peaks at 162.2 and 163.3 eV in S 2p spectra were ascribed to the S^{2-} state. TGA showed that

19   the amount of bile salts adsorbed on the 2D MoS_2 nanosheets was 13%, corresponding to 325

20   µmol/g (**Figure S4**).

21   These MoS_2 nanosheets suspended in 5% glucose at a concentration of 1 mg/mL were

22   nebulized into the trachea of healthy mice. Mice were sacrificed at days 0.5, 1, 2, 7, 14 and 28

23   after this single nanoparticle exposure and the BALF were collected and analyzed for their

24   immune cell distribution, protein content, inflammatory cytokines and extracellular vesicles

25   (**Figure 1b**). All these components can be involved as pro- and anti-inflammatory mediators

26   to regulate lung inflammation in case of injury.[40] Particularly cells of the innate immune

27   system such as macrophages or neutrophils play major roles in the early process of

28   inflammation and also influence other cells in driving pro-resolution against such

29   inflammation.[41] Total cells isolated from BALF increased at 12 h post-exposure to MoS_2

30   (pvalue = 0.0642), but were not significantly increased over one-month post-exposure to

31   MoS_2 compared to vehicle (**Figure S5a**). The adherent alveolar macrophages comprised the

32   majority of isolated BALF cells (around 95%) (**Figure S5d**), with an increase at 12 h

33   compared to the vehicle (pvalue = 0.0773) (**Figure S5c**). Neutrophils rapidly migrate towards

34   inflamed tissue upon inflammatory insult and can change their phenotype depending on the

inflammatory status. In the first hours after MoS_2 exposure, we observed a significant increase
of neutrophils in BALF, but this increase is not maintained after 1 day (**Figure S5b**), their
percentage in total cell population being rapidly reduced to near vehicle numbers (**Figure
S5f**). We did not observe any significant increase in total protein levels in BALF in
comparison to the vehicle controls (**Figure S5g)** nor higher leukocytes mortality (**Figure
S5h**). By contrast, experiments on the same model using lipopolysaccharide as positive
control, demonstrated that after intratracheal administration of 2 mg/kg of LPS a significant
increase in cell count was measured in the BALF 24 and 48 h after administration compared
to vehicle-instilled mice (2×10^7/mL at 48 h), with a significant mortality (1×10^7/mL), together
with a large proportion of neutrophils (80-90% at 24 and 48 h) (data not shown). However,
the cytokine profile revealed an impact of MoS_2 exposure which depends on the time after
exposure (**Figure S6a-b**). Notably, as shown in the heat map of mean fold-change signal
intensity versus control of cytokine array (**Figure 1c**), several proteins expression were
increased at 12 h post-exposure (e.g., Leptin, MIG, MIP-1-gamma and TIMP-1 have a fold
change > 1.5) or decreased (e.g., Axl has a fold change < 0.5), showing a trend to an
inflammatory profile at this time point, which is consistent with the increase of inflammatory
cells observed previously. Particularly, leptin could modulate neutrophil activity and function,
which correlates with the increased number of neutrophils at this time point. In contrast, at
day 1 and day 2 soon after exposure the expression of most of the proteins implicated in
inflammatory response were decreased compared to the control (e.g., Axl, Eotaxin, IGF-BP-5,
Il-1beta, IL12p40/p70, Leptin, L-Selectin, MIG, SCF, TIMP-1 and VEGF have a fold change
< 0.5). Globally, these results indicate a pro-inflammatory insult detected in the first 12 h after
MoS_2 nebulization, followed by rapid anti-inflammatory mechanisms that reduced the
production of pro-inflammatory mediators in mice BALF from 24 h and 48 h post-exposure.
For the later time points up to one month, there were few differences of protein expression as
compared to vehicle conditions, although the expression of some proteins were increased
(e.g., Il-2, IL-17 and KC with a fold >1.5). Consistent with the cellular and protein analysis,
we can conclude from cytokine analysis that MoS_2 lung exposure induces onset of
inflammation during the first 24 h, which is resolved in a couple of days after exposure
through a potent anti-inflammatory mechanism. At longer time points up to one-month post-
exposure, we observed a normalization of the BALF immune microenvironment, indicating
the durable resolution of inflammation and recovery of lung homeostasis.
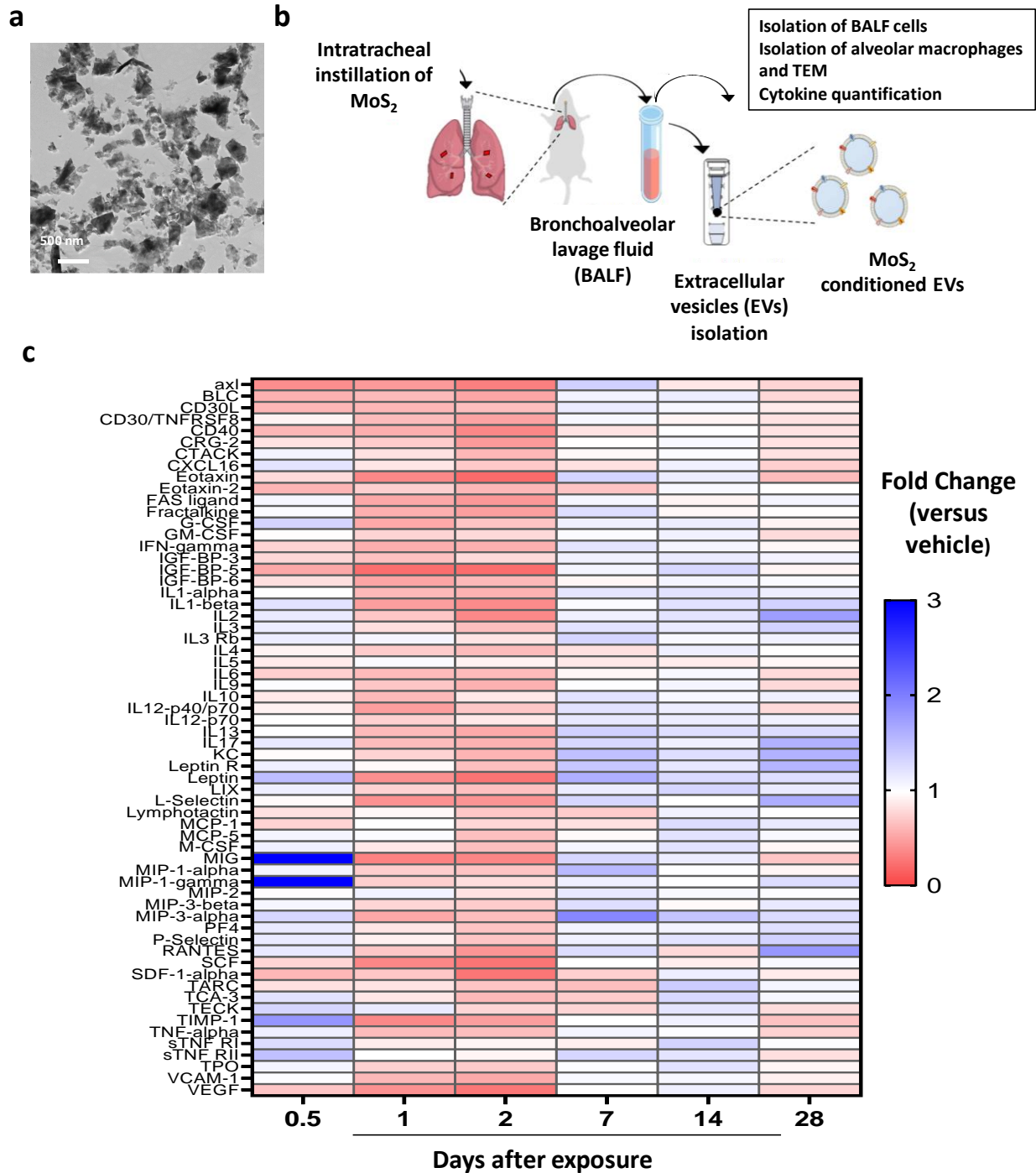
Figure 1. (a) TEM image of MoS_2 nanosheets before inhalation in mouse. (b) Experimental design of MoS_2 nanoparticles intratracheal instillation in mice and recovery and analysis of BALF. (c) Heatmap representing the mean fold change signal intensity of cytokine array in BALF of MoS_2-exposed mice versus non-exposed (vehicle) mice for each time-point after instillation. Number of mice: n=2 (0.5 day); n=3 (1 and 2 days); n= 1 (7, 14 and 28 days).
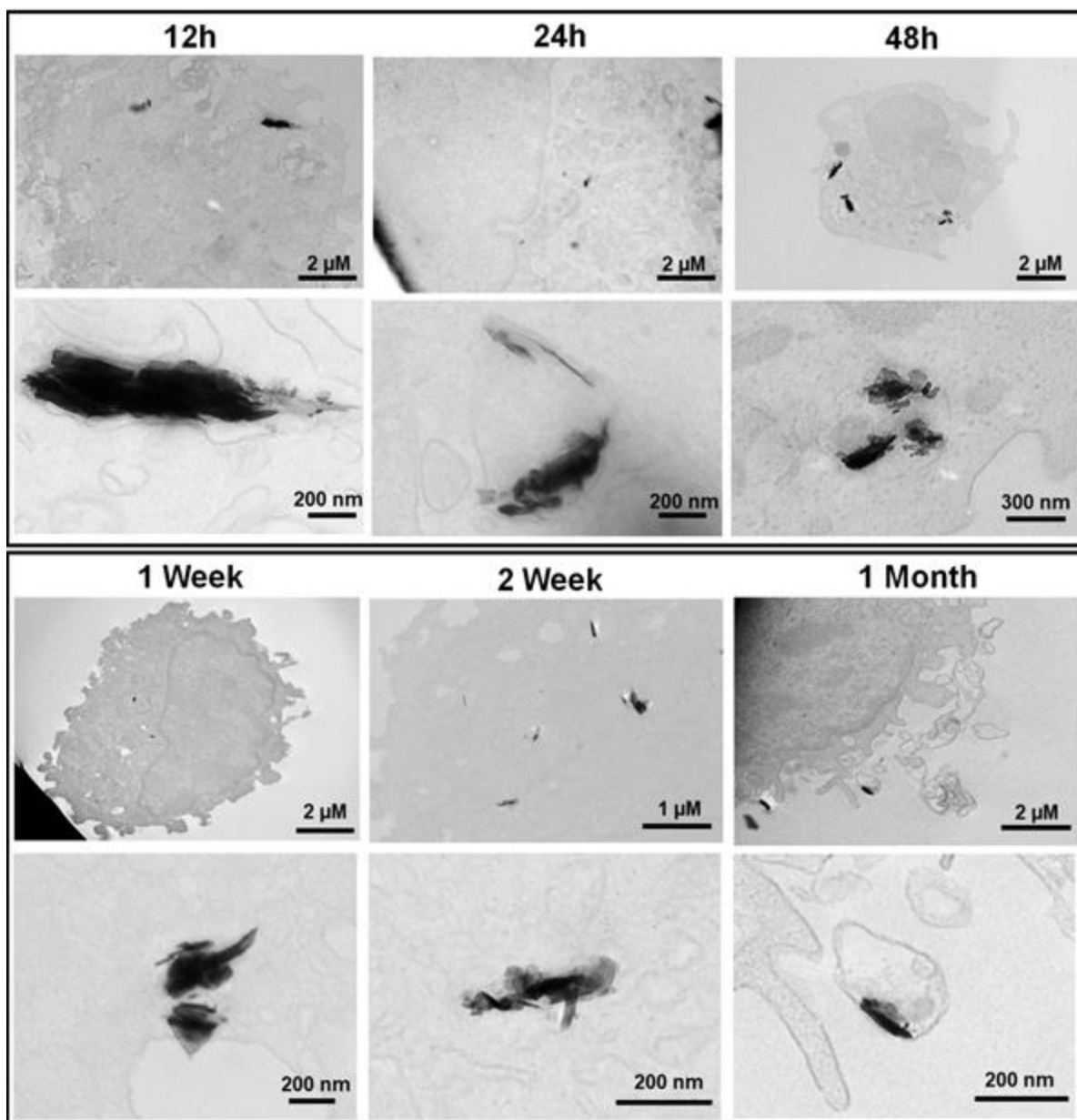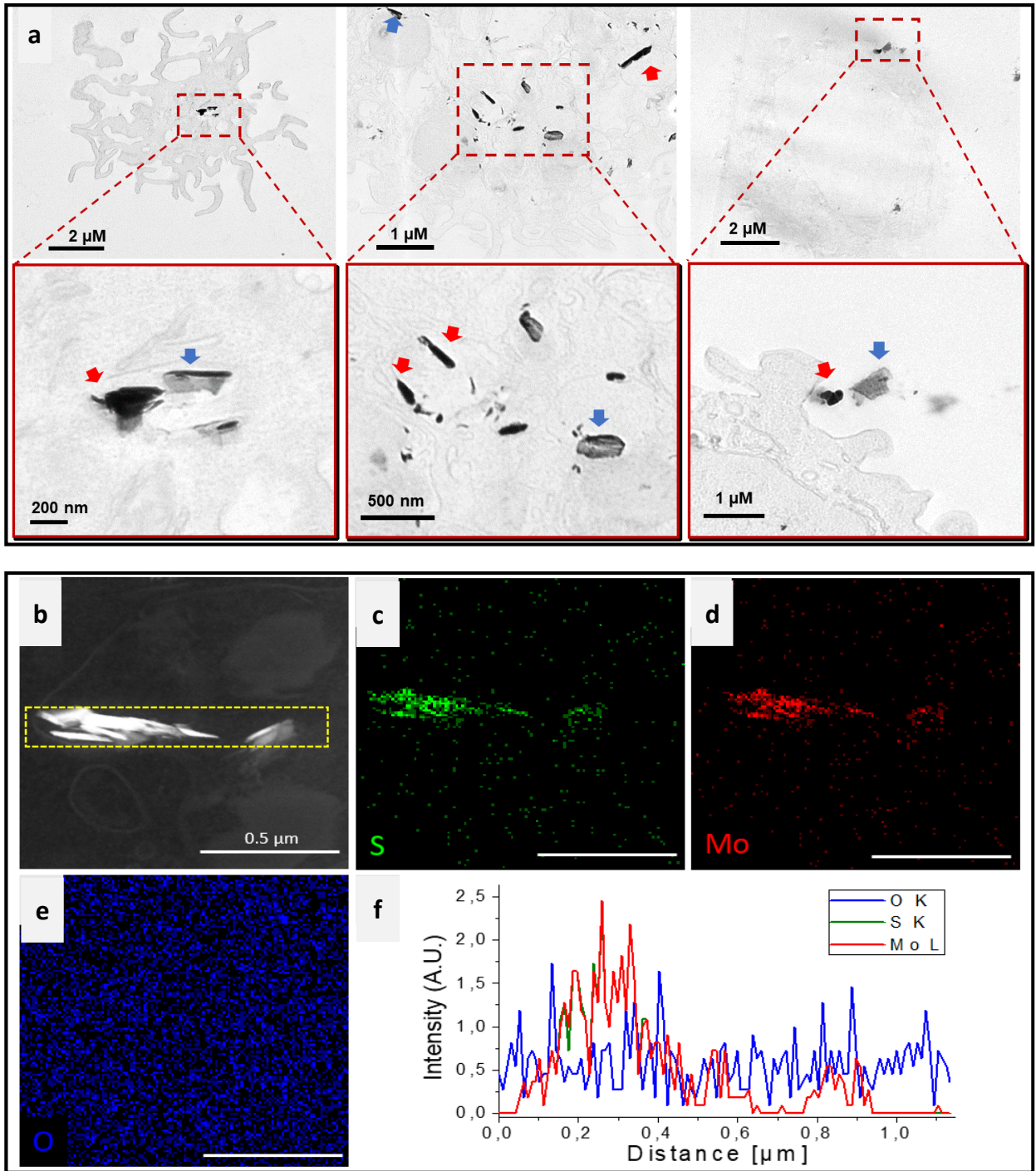
Figure 2. TEM images of alveolar macrophages recovered in BALF of MoS$_2$-exposed mice at different time-points after exposure. An extracellular vesicle containing MoS$_2$ is highlighted by a blue arrow.

To get insights into the mechanisms of nanoparticle processing and resolution of inflammation, we have combined a multiscale investigation looking both at the lung microenvironment response and at the (intracellular) transformation of the 2D nanoparticles. We isolated alveolar macrophages from BALF at predetermined time points after MoS$_2$ exposure and observed the nanoparticle distribution and morphology by TEM (**Figure 2**). Immediately after the first 24 h of exposure up to 1 month, we found internalized structures that are no longer flat MoS$_2$ nanosheets but rather different types of intracellular transformed

7

MoS$_2$, such as fully scrolled, half scrolled and fully folded sheets. Interestingly, we also observed the exocytosis of nanoscrolls via extracellular vesicles indicated by the blue arrow in **Figure 2**. As such biotransformation has not been described before, we investigated in more details the role and mechanisms of intracellular transformation of MoS$_2$ nanosheets and extracellular vesicle release in the lung homeostasis restoration following MoS$_2$ exposure.

2.1. MoS$_2$ nanoscroll formation in alveolar macrophages: a mechanism to mitigate the inflammatory insult?

In light of our observations we hypothesize that intracellular transformation of MoS$_2$, particularly nanoscroll formation, could serve as a cellular defense mechanism against the MoS$_2$-driven insult. MoS$_2$ is a layered structure, in which the number of layers and their orientation could have toxicological implications, depending on the surface area and active edge sites that interact with the biological environment. Indeed, *in vitro* study conducted with MoS$_2$ nanosheets proved that the extent of exfoliation is correlated with the cytotoxicity of the nanosheets.[39] Therefore, we thought to investigate the dynamic interactions of MoS$_2$ nanosheets with alveolar macrophages that were isolated from BALF of unexposed mice. AMs are tissue resident macrophages which are directly exposed to the environment and thus play an important role in immune regulation occurring due to inhaled foreign pathogens.[42] These primary AM were exposed *ex vivo* with 20 µg/mL MoS$_2$ for 12 h. In line with AM observations after MoS$_2$ inhalation *in vivo*, cells exposed *ex vivo* showed the same type of scrolled sheets embedded within intracellular structures, presumably endo-lysosomes (**Figure 3a**). Scrolling was complete (red arrow) or partial (blue arrow), finding some sheets scrolled only at the edges. EDX elemental mapping shows that the nanoscrolls are composed of Mo and S, with no increase in the amount of oxygen over the scrolls. Thus, EDX analysis did not point to the oxidation of the surface (**Figure 3b-f**).

Figure 3. TEM images of primary alveolar macrophages exposed *ex vivo* to MoS_2 nanoparticles for 12 h. Intracellular or extracellular fully scrolled (red arrows) or half-scrolled (blue arrow) MoS_2 can be observed. (b-f) EDX elemental mapping of an intracellular MoS_2 scroll: (b) bright field image of the intracellular nanoscrolls, (c) sulfur, (d) molybdenum, (e) oxygen map, and (f) relative intensity profile.

2.2. Tracking oxidative stress-induced MoS₂ transformation *in situ* with liquid TEM

To mimic the mechanisms driving MoS₂ biotransformation within intracellular organelles, we decided to track the dynamic behavior of MoS₂ at the nanoscale using *in situ* liquid TEM under conditions that are relevant to the harsh environment of degradation compartments such as lysosomes. We considered the elevated production of ROS including superoxide ($O_2^{\bullet-}$), and hydroxy radicals ($HO^{\bullet}$) in inflamed tissues,[43,44] and typical concentrations of H_2O_2 around 0.05 - 0.1 mM, within the lysosomes that are responsible for the degradation of xenobiotics and undesirable proteins or protein aggregates. However, degradation of MoS₂ has shown to take several weeks up to a month tracked by *in vivo* studies.[15] Therefore, for the *in situ* studies H_2O_2 concentration in the biomimetic media has been set to be around hundred times higher, 5-10 mM, to have a faster degradation process traceable in a shorter timespan within the microscope. Additionally, a DPBS solution was used to simulate the saline conditions in biological systems.

2.2.1. Scrolling

When dispersed in the DPBS-H_2O_2 solution, early observation of stacked patches revealed a further spreading of the few layers of MoS₂ stacks (**Figure 4a**, **Movie S1**). This increase of interlayer distance is probably promoted by the presence of different cations coming from the buffer mixture known to intercalate in between the MoS₂ layers.[45] The further spreadsheets tend to fold and scroll in a very fast process that takes place in a few seconds as evidenced in **Figure 4a** pointed by the yellow arrows or in **Figure 4b (Movie S2)** for a single nanosheet. The initial exfoliation-intercalation process can be at the origin of the rolling up. Similar intercalation using organic solvents has been described to promote the scrolling of MoS₂ flakes.[46] Free standing sheets in the liquid have a low folding barrier.[47] Furthermore, strain energy can be induced more easily by a dynamic behavior of sulfur atoms at the surface of the freestanding sheets.[48] Molecular dynamics simulations have evidenced the impact of desulfurization percentage in the morphological changes of freestanding MoS₂,[49] that fully coincide with the scrolling process we have observed *in situ* as well as in the alveolar macrophages exposed to MoS₂ *in vivo* and *ex vivo*. The previous simulation predicted that the sheets tend to form scrolls to minimize the surface energy when there is a high depletion (>40%) of S atoms. Indeed, post-*in situ* HR-TEM observations show some structures that match the simulated structure for scrolled sheets with a desulfurization degree of ~60% (**Figure 4c**).[49] Interlayer distances in the scrolls vary from 0.55 to 0.61 nm (**Figure 4d-e**), which is in the range between typical nanotubes and bulk MoS₂.[50] The *in situ* liquid experiments and *post-in situ* TEM in **Figure 4** put in evidence that the sheets tend to wrinkle,

1   fold and finally scroll from the corners rather than the edges. Nonetheless, scrolls tend to be

2   found in partially unfolded sheets as well, which might be related to the degree of

3   desulfuration. The scrolling process showed to be reversible (**Movie S3**). The reversibility of

4   the scrolling points to preservation of the MoS_2 structure, since there is not an appreciable

5   increase in the oxygen content as confirmed by the *ex vivo* TEM analysis (**Figure 3**).
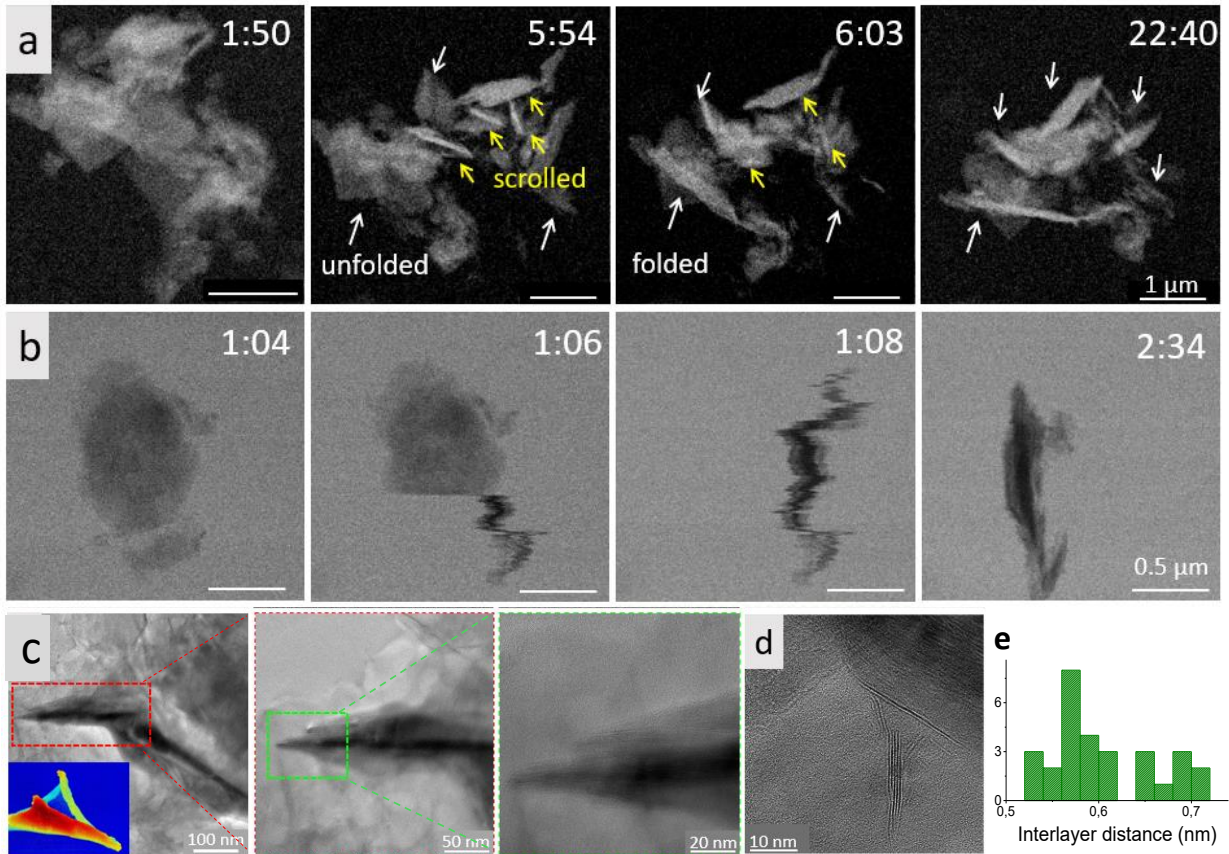
6

7   **Figure 4.** (a) STEM image sequence from *in situ* liquid phase recording of MoS_2 sheets in 10

8   mM H_2O_2-DPBS. The white and yellow arrows point to sheets that fold and those that

9   scrolled, respectively. (b) STEM image sequence from *in situ* liquid phase recording of free-

10   standing MoS_2 patch scrolling in 5 mM H_2O_2-DPBS. Time is indicated in min. The last two

11   panels on the right side show the intermediate stages between a free-standing sheet and a fully

12   scrolled needle. These are extracts of movie S3. (c) Nanoscrolls observed after the *in situ*

13   experiments. Inset corresponds to the predicted structure for scrolled sheets with a

14   desulfurization degree of ~60%.[49] (d) HR-TEM image of a MoS_2 nanoscroll and (e)

15   histogram of interlayer distance.

16

17   Thereby, we have shown that MoS_2 nanosheets form dynamic nanoscrolls as filmed in **Movie**

18   **S3**. In the literature, this scrolling process has been described primarily in CVD-deposited

19   sheets.[48] Controlled scrolling of MoS_2 has been achieved by different approaches including

1 plasma bombardment, solvent drying and electrochemical folding. [46,47, 50] However, this

2 process has never been observed concomitantly *in situ* in biomimetic oxidizing medium and

3 *in vivo* or *ex vivo* in alveolar macrophages as a mechanism of intracellular processing.

4 *2.2.2. Etching*

5 In addition to the scrolling, we found that the unfolded sheets can undergo oxidation and

6 etching which is the typical degradation pathway of MoS_2 in the presence of H_2O_2.[51] MoS_2

7 has been shown to dissolve in oxygenated aqueous media releasing molybdate ions as

8 described in equation (1):[15,16]

9 $MoS_2 + 9/2 O_2 + 3H_2O \rightarrow MoO_4^{2-} + 2SO_4^{2-} + 6H^+$ (1)

10 Here we were able to track in real-time the etching process within the biomimetic media. A

11 representative sequence of the etching is presented in **Figure 5.** The etching speed observed in

12 the *in situ* experiments is probably exacerbated by the electron beam illumination. The patch

13 edges are etched gradually from edges inwards evidencing a change in the aspect ratio from

14 1.26 at 33 s up to 3.47 by 227 s (**Figure 5a**, **Movie S4**). Notably, the etching is faster in the

15 direction perpendicular to the zigzag edges as evidenced in **Figure 5b**. Oppositely, facets

16 developed at 90° which correspond to the armchair edges, tend to disappear upon etching

17 progression. This observation is in agreement with DFT studies and previous controlled

18 etching experiments pointing to higher stability for the zigzag edges in comparison with the

19 armchair.[52,53] Furthermore, the sheets can also etch internally through defects at the surface

20 (**Figure 5c**, **Movie S5**). The internal etching path is probably dominated by the presence of

21 defects at the surface of the layers leading to the further exposure of new zigzag edges in the

22 inner regions (**Figure 5d**).

23
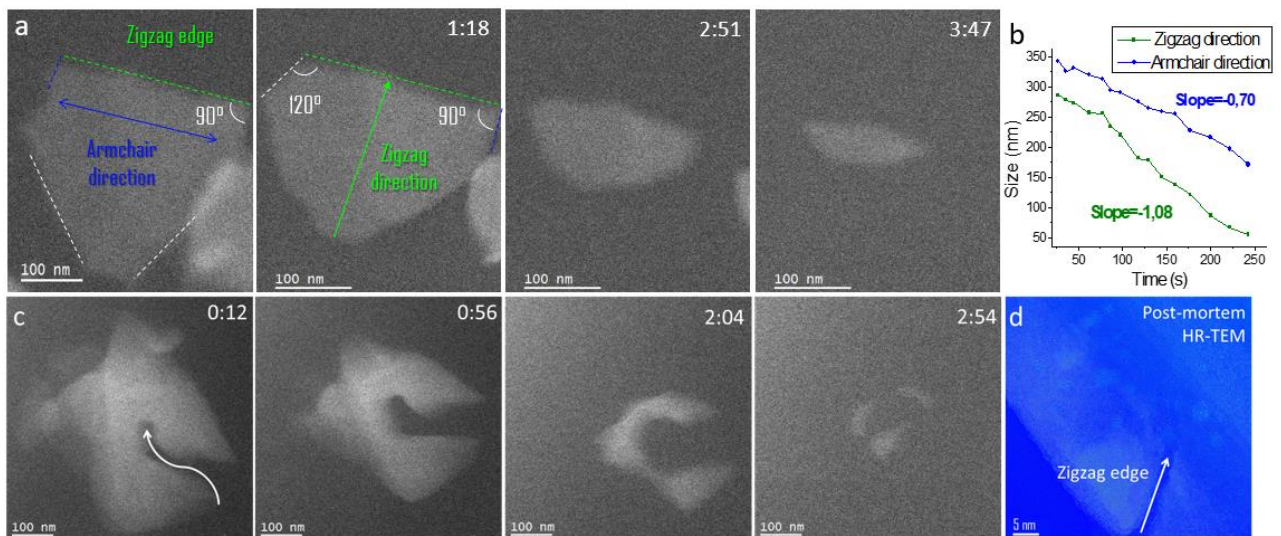
24 **Figure 5.** (a) STEM sequence from *in situ* liquid etching of MoS_2 sheets in DPBS-H_2O_2

25 solution. (b) Size change in the zigzag and armchair directions of a sheet over time. (c)

Sequence from *in situ* liquid STEM displaying internal etching from edge defects of a single MoS$_2$ sheet. (d) Post-*in situ* HRTEM image of the etching pathway exposing zigzag edges.

2.2.3. Oxidation

The etching is likely induced by the oxidation mechanism described in the previous section leaching ions into the liquid. However, we evidenced another oxidation process. In contrast with the etching described above, the layered structure can remain upon surface oxygen adsorption leaving oxidized fragments like those found in samples degraded in our experiments *in situ* (**Figure S7a**). The corresponding Fast Fourier transformation of HRTEM of such fragments confirmed the oxidation to MoO$_3$ which has been shown to be the product of MoS$_2$ oxidation by different synthesis methods,[54,55] and by a previous study on the enzymatic degradation of MoS$_2$.[15,19] Interestingly we observed the same diffraction patterns of MoO$_3$ in fragments found within extracellular vesicles of *ex vivo* AMs after 24 h exposure to MoS$_2$ (**Figure S7b**). Such oxidation has been described in the literature to take place in the presence of low concentrations of H$_2$O$_2$ (1%, 3% and 6%).[15,19,51] This observation suggests that in conditions closer to those of biological media, the MoS$_2$ sheets could also preserve its layered structure and get oxidized on the surface.

To sum up, three main transformation mechanisms were observed directly at the nanoscale thanks to the *in situ* liquid phase STE experiments: 1) scrolling of the dispersed sheets; 2) etching releasing soluble degradation products in solution; and 3) oxidation generating oxidized sheet fragments or nanoparticles.

We would like to underline that our experiments were performed at room temperature and in buffered conditions (e.g., 25°C, pH 6-7). We expect that changes in the temperature and pH of the solution would have different effects on the in situ transformation of MoS$_2$ depending on the process induced by the presence of H$_2$O$_2$. At temperatures below 60° C the disproportionation of H$_2$O$_2$ is slow,[56] so the etching and oxidation following equation (1) will be probably constant with a continuous influx of H$_2$O$_2$, and above this temperature the etching rate would slow down upon disproportionation. Furthermore, it has been shown that at higher temperatures, upon etching the exposed facets of MoS$_2$ can change from triangles to shapes with hexagonal holes above 600 °C.[53] In regards to the impact of different pH conditions, studies tackling the colloidal stability of MoS$_2$ at various pH values have shown that MoS$_2$ stability diminished only in solutions at pH below 1.9.[16] Therefore, even in typically acidic lysosomal medium where the pH can be around 4.5-5, we do not expect a significant impact on the overall observed processes. On the other hand, if the change in the

pH is due to higher concentrations of H_2O_2, we could expect an exacerbation of the etching and oxidation processes. Based on our and other observations,[57] hydrogen peroxide tends to spontaneously induce the exfoliation of MoS_2 enabling probably more free-standing sheets to scroll and fold up. We also showed in the *in situ* STEM experiment that the scrolling, etching and oxidation of free-standing sheets have accelerated kinetics, where the concentration of H_2O_2 is up to 100 times higher than that of biological media. Thus, while these processes take from days to several weeks in cellular organelles, the *in situ* STEM observations were carried out only on in the time frame of tens of min.

Considering the similar observations of MoS_2 scroll, etching and oxidation in *in vivo* or *ex vivo* exposed alveolar macrophages, the *in situ* dynamic observations of these processes could be relevant to the intracellular transformation of MoS_2 in the lysosome environment. The scrolling process was not observed so far. On the other hand, while etching and oxidation processes were expected as a consequence of the interaction of MoS_2 with the different ROS and especially with H_2O_2, deepened structural insight was accessed into the etching and oxidation processes. Considering that such intracellular fate of MoS_2 in alveolar macrophages was associated with a rapid and concomitant resolution of the initial acute inflammation, intracellular ROS could indeed be used by cells as a detoxification mechanism to pronounce scrolling, etching, and oxidation and to significantly reduce the active surface area, dimensions, and edge sites, where the presence of dangling bonds can be highly active sites.[58-60] This hypothesis is reinforced by our data showing the nanoscroll formation from the edges and low surface oxidation.

2.3. 2D MoS₂ exerts transient oxidative stress and pro-inflammatory effects *in vitro*

To get deeper insight into the cellular effect of MoS_2 on the monocyte/macrophage system, we investigated the inflammatory response of THP-1 cells, an in vitro model cell line of human monocytes that can be also differentiated into macrophages. Particularly, THP-1 dual reporter cells possess inducible reporter constructs allowing to investigate both NFκB (nuclear factor kappa light chain enhancer of activated B cell) and interferon (IFN) inflammatory pathway activation. NFκB is one of the key regulatory pathways in nanomaterial-induced oxidative stress, which could lead to cell damage and apoptosis. Toll-like receptor 4 (TLR4) signaling initiates translocation of NFκB into the nucleus from the cytoplasm to induce gene transcription contributing to the pattern of inflammatory gene expression. In addition, IFN regulatory factor 3 (IRF3) is a crucial transcription factor implicated in promoting systemic pro-inflammatory responses.

Firstly, the metabolic mitochondrial activities of THP-1 macrophages (**Figure S8a**) and THP1 dual monocytes were assessed by Alamar Blue assay after 24 h exposure to different concentrations of MoS_2. None of the tested concentrations could directly affect the cell metabolic activity. We thus examined the immunostimulatory activity of MoS_2 on THP-1 dual monocytes. Positive controls of NFκB and IFN activation were represented by LPS exposed cells in **Figure 6**. Dual THP-1 monocytes were exposed to MoS_2 nanosheets for 24 h to 72 h (**Figure 6a)** inducing a concentration-dependent NFκB activation at 24 h post-exposure in a significant manner (**Figure 6b)**. Importantly, the dose-dependent NFκB activation was reduced after 72 h incubation (**Figure 6d)**. IFN pathway was instead not significantly triggered even at higher concentrations of MoS_2 (**Figure 6c, e**). Oxidative stress is one of the key mechanisms by which inhaled particles mediate pulmonary inflammation. *In vitro* oxidative stress experiments were thus conducted using a 2',7'- dichlorofluorescein diacetate (DCFH-DA) assay to measure intracellular ROS on THP-1 macrophages (**Figure S9**). We observed increasing ROS generation due to the aging of macrophages over time, which was however exacerbated by MoS_2 nanosheets (2 folds) at 24 h incubation. However, at later incubation time points, the increase of ROS generation over time was mitigated by MoS_2 (up to 50% lower than for control) independently of the nanosheet concentration. These protective effects on ROS generation together with the reduction at 72 h of NFκB activation suggest that self-defense pathways and pro-resolutive mechanisms against inflammation could be activated upon MoS_2 internalization, intrinsically related to the intracellular transformations (scrolling, edging and oxidation) reported above. In particular, we evidenced with *in situ* liquid phase STEM that oxidative species were used for scrolling and etching of MoS_2 nanosheets. It is known that the transcription of NFκB-dependent genes influences the levels of ROS in the cells, and in turn, NFκB activity can be regulated by the levels of ROS. Here the interplay of NFκB signaling pathways, ROS generation, and consumption for MoS_2 intracellular transformations can be considered as an efficient mechanism of defense against MoS_2 nanosheet-induced cell injury. Such mechanisms of self-defense against nanoparticles through ROS-induced intracellular transformation and degradation into safer forms have been demonstrated before for carbon nanotubes,[31] and gold nanoparticles.[35]
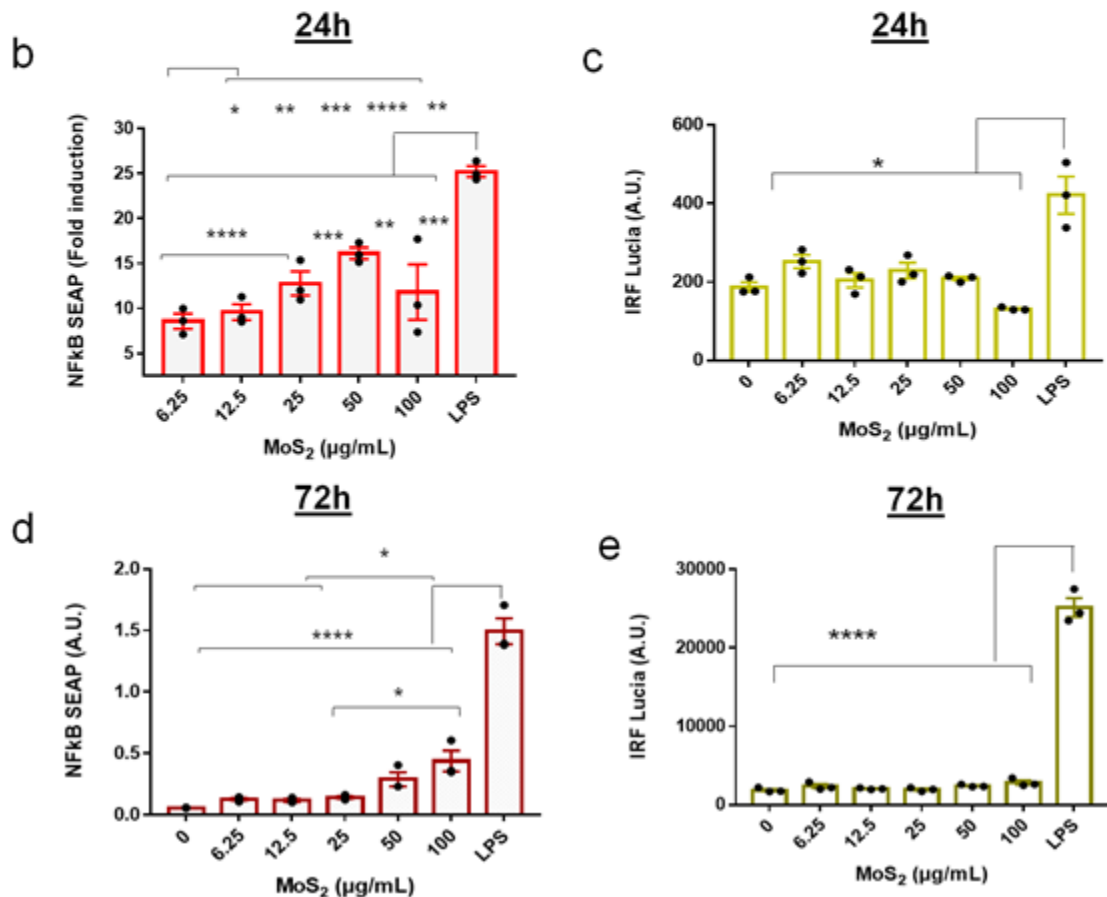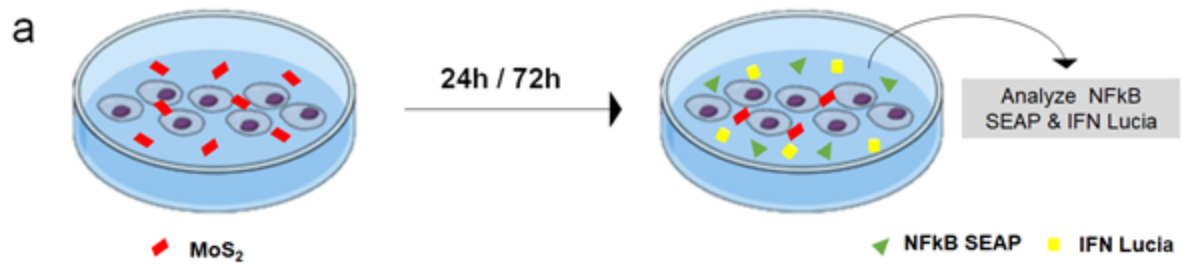
Figure 6. (a) Schematic showing the experimental plan for determining the inflammatory status of THP-1 dual monocytes upon MoS_2 treatment at different doses for 24 h or 72 h. NFκB & IRF3 pathway induction were analyzed by quantifying NFκB SEAP (b, d) and IFN Lucia (c, e) in the supernatant 24 h after incubation. The positive control was represented by LPS-exposed cells for 24 h or 72 h. Statistical significance was calculated using one-way ANOVA (Tukey's multiple comparison test). * represents $p< 0.05$; ** represents $p< 0.005$; *** represents $p=0.0005$, and **** represents $p<0.0001$.

2.4. Alveolar extracellular vesicles as mediators of inflammation resolution

In the outcome of MoS_2 exposure, we noticed the presence of EVs released in BALF or by alveolar macrophages, some of them containing transformed MoS_2 nanoparticles (**Figures 2**, **3a** and **Figure S7**). EVs are recognized as key mediators in cell-to-cell communication in response to xenobiotics and infection with the ability to shuttle biological signals playing a central role in lung inflammatory response.[61] We and others also discovered that EVs released by nanoparticle-exposed cells can transfer carbon nanotubes, iron oxide, gold or titanium dioxide nanoparticles to naïve cells, with nanoparticle specific outcomes on recipient cells.[29,31,36] Hence we made the hypothesis that EVs in BALF could play a role in the dissemination and/or detoxification of MoS_2 from alveolar macrophages and could also modulate the inflammation process in addition to soluble factors such as cytokines. In order to investigate the role and quantity of EVs in BALF, EVs were isolated from BALF at different time points after exposure using ultrafiltration (**Figure 1b**). EV concentration and size distribution were determined by nanoparticle tracking analysis (NTA) (**Figure 7a**, **b**, **c**) showing a decreasing number of BALF EVs with increasing time after inhalation, both in MoS_2 exposed and non-exposed mice, and similar average EV sizes over time. NTA diameter distribution ranged from 60 nm to 200 nm as illustrated in **Figure 7c** for BALF EVs from MoS_2 exposed mice at 24 h. EVs were also observed by TEM with negative staining showing a similar vesicular aspect in exposed and non-exposed mice and an average diameter of 50±4 nm for MoS_2 exposed mice compared to 60± 4 nm for control mice at 24 h (**Figure 7d**). Such small EVs (<60 nm) observed by TEM are not detected by NTA and could contribute to an unquantified proportion of the EV population. Overall, there was a tendency to lower sizes of MoS_2 exposed BALF EVs compared to EVs of control mice. Specific transmembrane tetraspanin markers of EVs were also characterized using the Exoview® platform, which detects both the interferometric signal and fluorescence signal of EVs that bind to specific antibody spots printed onto a microarray chip (**Figure 7e-g**). **Figure 7e** illustrates the specific immuno-capture of EVs from BALF of MoS_2-exposed mice at 24 h on an anti-CD9 chip and the presence of CD9 (blue), CD63 (red) and CD81 (green) tetraspanin markers stained by their associated fluorescence antibody. **Figure 7f** displays the quantitative comparison between the EV groups deposited on the chip at the same concentration based on NTA measurement. All BALF EVs express CD9 and CD81 antibodies regardless of the time points after exposure. We note a tendency towards a higher expression of CD9 and CD81 for BALF EVs of MoS_2 at 24 h. The EV mean diameter determined from the interferometric signal on

17

anti-CD9 or anti-CD81 chip is consistent with the diameter determined by TEM around 60 nm whatever the conditions (**Figure 7g**).
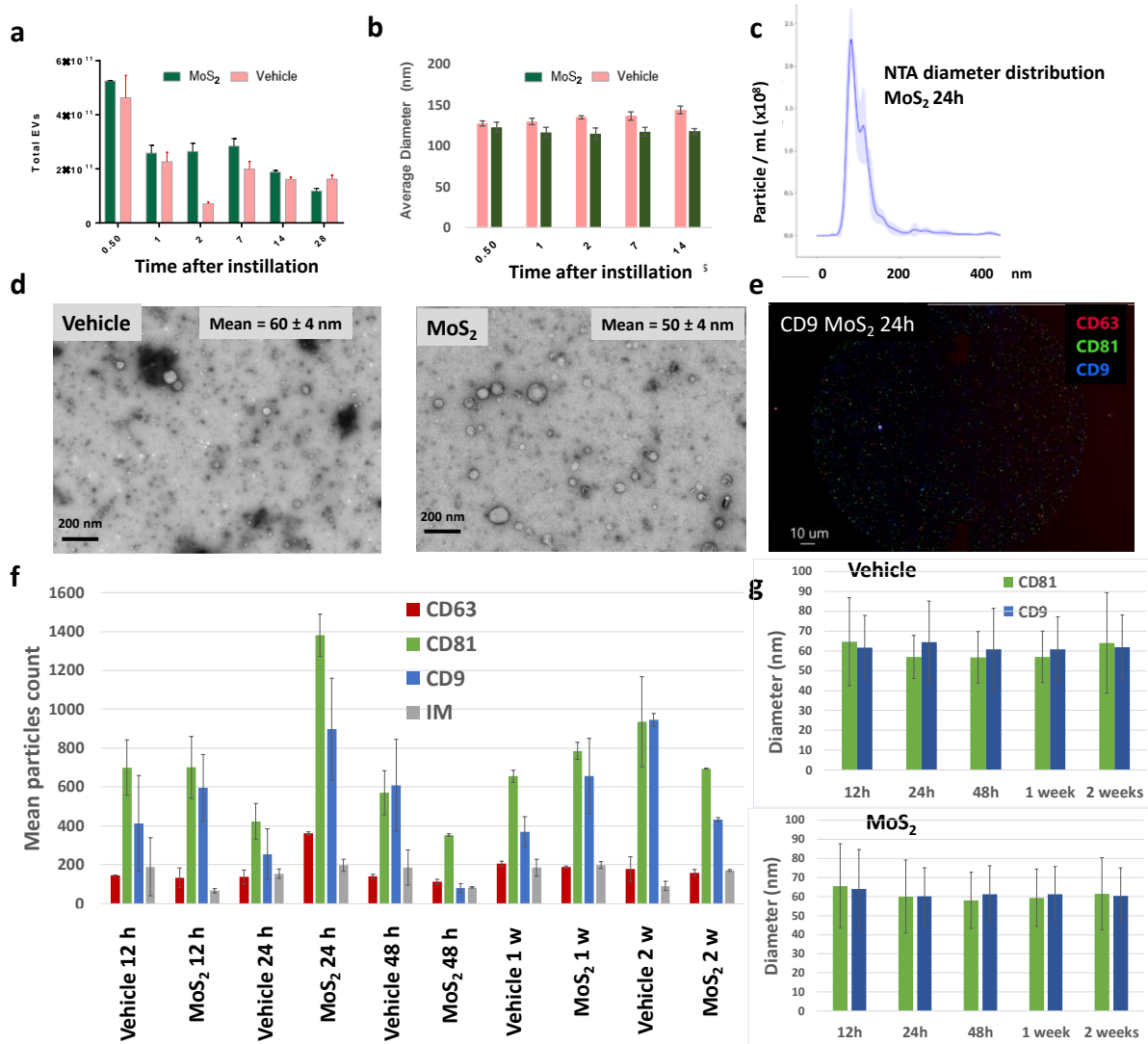

Figure 7. Characterization of EVs isolated from BALF of MoS_2-exposed and non-exposed (vehicle) mice at different time points after exposure. (a) Total number of EVs isolated from BALF and quantified by NTA. (b) Average diameter of EVs determined by NTA. (c) Example of particle size distribution by NTA for BALF EVs of MoS_2-exposed mice 24 h after exposure. Error bars in (a) and (b) are the results of three independent measurements. (d) Electron micrographs of BALF EVs after negative staining. The mean diameter of vesicles is indicated in inset. (e) Immunofluorescence microscopy of single BALF EVs (MoS_2, 24 h) captured on anti-CD9 antibody-coated chip with Exoview® platform and stained using anti-CD81 (green), anti-CD63 (red), anti-CD9 (blue) fluorescent antibodies, (f) Quantification of single fluorescence spots (anti-CD81, anti-CD9 and anti-CD63 immunostaining), or interferometric spots (IM) detected on anti-CD9 coated chip exposed to BALF EVs. (g)

18

1 Average diameter of BALF EVs captured on anti-CD9 or anti-CD81 chip and detected by

2 interferometric signal.

3

4 To investigate the role of BALF EVs and the intercellular communication in the modulation

5 of inflammation, we tested the inflammatory NFκB and IFN pathways of Dual THP-1

6 monocytes in response to BALF EV exposure. We first examined the impact of BALF EVs

7 on THP-1 Dual monocytes (1×10^9 EVs for 80000 cells) in the absence of inflammatory

8 activation (**Figure 8a**). Positive control corresponds to LPS-exposed cells. The results

9 indicate that the NFκB pathway in THP-1 monocytes was activated by BALF EVs at

10 intermediate time-points (2 and 7 days) (**Figure 8b)**, but not the IFN pathway (**Figure 8c**).

11 However, the data point out a tendency towards reduced NFκB activation effect of EVs from

12 MoS_2-exposed mice compared to control EVs in the first two weeks after MoS_2 exposure.

13 Next, we tested the effect of the same EV dose incubated for 4 h on THP-1 dual monocytes

14 before subsequent activation by LPS for 24 h mimicking inflammatory insult (**Figure 8d**).

15 Interestingly, in comparison with LPS alone, the pre-treatments with EVs from MoS_2-exposed

16 mice at 12 h and 24 h post-exposure significantly counteract the inflammatory effect of LPS

17 (**Figure 8e, f**). This anti-inflammatory effect was not observed at these early time-points with

18 EVs of non-exposed mice. The inflammatory inhibition activity of EVs from MoS_2 exposed

19 mice could reach 50 % for NFκB activation in comparison to non-exposed mice (**Figure 8e**).

20 Similarly, there was a significant reduction in IFN pathway activation at the early time points

21 in comparison to non-exposed mice (**Figure 8f)**. It is important to note that this defense

22 mechanism mediated by EVs from exposed mice is particularly revealed in combination with

23 external stress such as LPS, but less in bare treatment with EVs alone on inactivated

24 monocytes. This reveals that EVs from MoS_2-exposed mice can exert anti-inflammatory

25 properties that are particularly potent at 12 h and 24 h after exposure compared to the control

26 mice. Although EVs from exposed and non-exposed mice have a similar concentration in

27 BALF and share rather similar morphology, sizes, and tetraspanin markers (except at the 24 h

28 time-point), nanoparticle insult changes the immunomodulatory properties of BALF EVs on

29 monocytes *in vitro*. This suggests that EVs in BALF (some of them with MoS_2 cargo) could

30 also play a role *in vivo* in driving inflammation resolution and re-establishing the homeostasis

31 via transfer of EV-mediated defense machinery. As we observed MoO_3 fragments as well as

32 partially or totally scrolled MoS_2 nanosheets in EVs found close to the alveolar macrophages

33 by electron microscopy, we cannot exclude that molybdenum EV cargo could shape the EV

34 immunomodulatory properties. Exocytosis efflux of MoS_2 nanosheets from cancer cells was

1 previously observed, and an anti-exocytosis strategy could enhance the anti-cancer

2 photothermal efficacy of MoS_2 nanosheets both *in vitro* and in cancer model *in vivo*.[62]

3 Moreover, it was reported that Raman spectroscopy follow-up of the fate of MoS_2 nanosheets

4 in macrophages pointed out an increase in the production of lipid bodies as a mechanism of

5 defense following exposure to MoS_2.[63] However, we could not detect molybdenum traces by

6 EDX in EVs retrieved from BALF at the different time points, indicating the scarcity of

7 molybdenum cargo in EVs. Therefore, it is more likely that the majority of EVs in BALF do

8 not transport MoS_2 nanosheets or their degradation products but are reshaped in their

9 molecular content to exert anti-inflammatory properties in response to MoS_2 exposure.
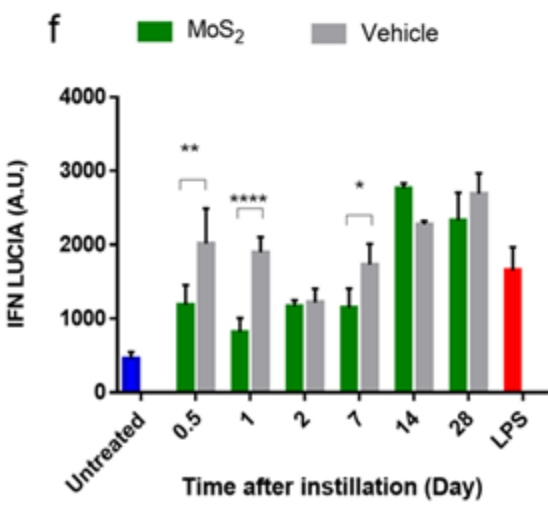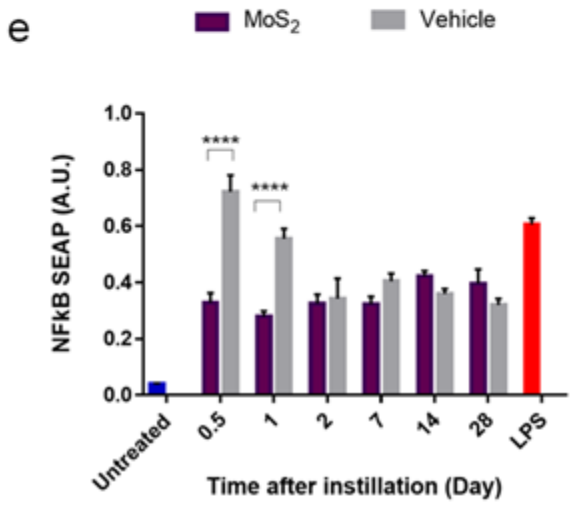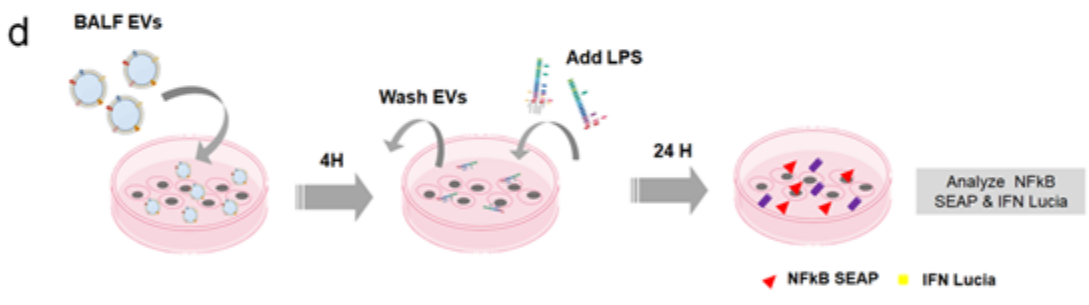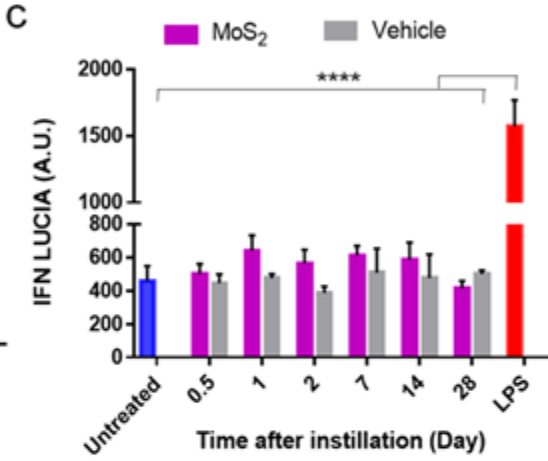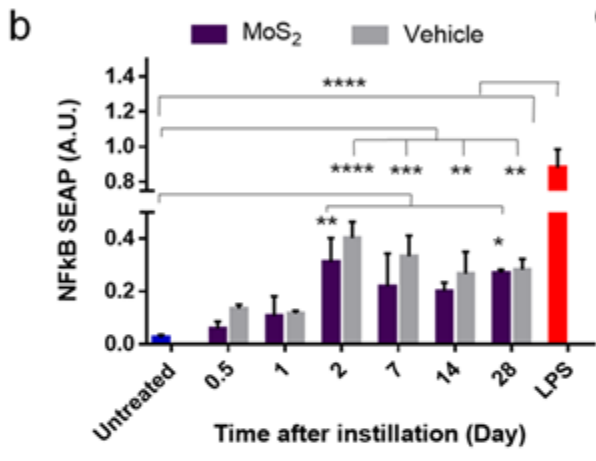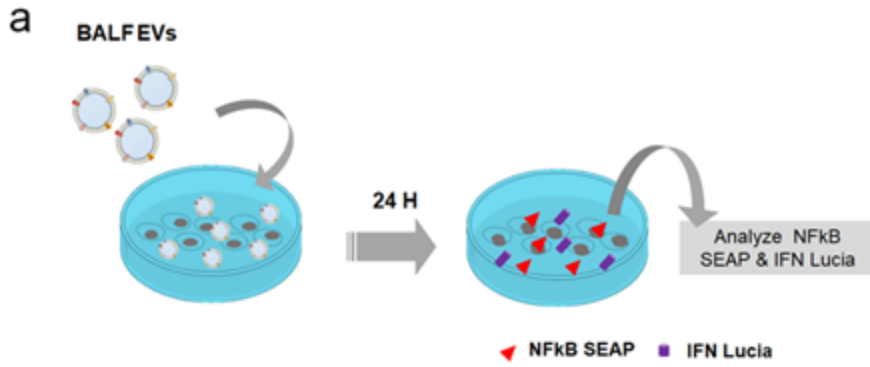
Figure 8. (a) Experimental design to assess the modulation of inflammatory pathway in THP-1 dual monocytes by BALF EVs. EVs from BALF of MoS_2 exposed and non-exposed (vehicle) mice at different time points after exposure were incubated for 24 h with THP-1 dual monocytes and the NFκB & IRF3 pathway induction were analyzed by quantifying NFκB SEAP (b) and IFN Lucia (c) in the conditioned medium. The positive control consists of THP-1 monocytes activated by LPS for 24 h. (d) Experimental design to assess the role of BALF EVs in regulating inflammation induced by LPS. EVs were first incubated with THP-1 dual monocytes for 4 h and rinsed before activation by LPS for 24 h and quantification of NFκB SEAP (e) and IFN Lucia (f) in the conditioned medium. LPS control represents THP-1 activated with LPS for 24 h without pre-incubation with EVs. Statistical significance was calculated using one-way ANOVA (Tukey's multiple comparison test).

3. Conclusion

In conclusion, we have examined the inflammatory status of the lungs of healthy mice up to one month after a single inhalation of MoS_2 nanosheets. We have proposed an integrated multiscale approach following simultaneously the fate and biotransformation of MoS_2 flakes at the nanoscale in the lung environment and the biological response to the nanoparticle exposure by a comprehensive analysis of BALF components. Our study demonstrates that MoS_2 nanosheets at a dose of 50 µg stimulate a rapid initiation of an acute inflammation, followed by its fast resolution in mouse lungs a few days after administration. BALF has been analyzed up to one-month post-exposure, showing the fast decrease of neutrophil population and persistent biotransformed molybdenum-containing nanostructures in alveolar macrophages and extracellular vesicles. To get insight into the dynamics of MoS_2 intracellular biotransformation at the nanoscale, *in situ* liquid phase STEM experiments were performed revealing three different ROS-dependent transformation mechanisms, consistent with the observation of nanostructure transformation in alveolar macrophages and EVs: 1) scrolling of the dispersed sheets leading to the formation of nanoscrolls and folded sheets; 2) etching releasing soluble degradation products in solution, most likely oxide ions (MoO_4^-); and 3) oxidation generating oxidized fragments. These mechanisms are representative of some of the various transformation products depicted from *in vivo* observations. Such direct and dynamic observation of the scrolling, etching and oxidation processes of MoS_2 nanosheets in a biological mimicking environment provides a direct insight into the intracellular processing of such 2D materials. It also suggests that the biotransformation processes rapidly consume reactive oxygen species in an attempt to manage cytotoxicity and withstand the internalization

1   of MoS$_2$ by alveolar macrophages transforming the nanosheets into less reactive and probably

2   safer forms while resolving inflammation.

3   Besides, it is still not clear if the transformed nanosheets are eliminated from the lung in the

4   long term and what would be the outcome of a repeated or chronic exposure in the lung, and

5   in the organs of the reticuloendothelial system, for example in the liver. Cao et al. have shown

6   that the biotransformation of MoS$_2$ nanodots leads to incorporation of molybdenum into

7   molybdenum enzymes, increasing their specific activities in the liver. This behaviour suggests

8   that long-term biotransformation of nanomaterials may have undesired effects on the

9   metabolism of this organ.[18] Our study only focused on the primary response of lung to a

10   single dose of MoS$_2$ as we observed this rapid resolution of inflammation and the unexpected

11   pro-resolving roles of EVs. Further studies are needed to explore the impact of repeated

12   exposure to MoS$_2$ and long-term effects (up to 6 months), to acquire more information on the

13   risk assessment (e.g., toxicity, pro-inflammatory effect, systemic effect, etc.) concerning

14   potentially exposed people.

15   The present study cannot conclude on the innocuity of the material or even on its long-term

16   fate. However, we have evidenced unprecedented mechanisms of intracellular

17   biotransformations and exportation via EVs of immunomodulatory signals from nanoparticle-

18   exposed cells. It might happen that under repeated exposure and/or higher doses, those

19   mechanisms of nanoparticle transformation and inflammation regulation, that are efficient

20   after a single exposure in our experimental set up to resolve inflammation, could be

21   overwhelmed. Nevertheless, such mechanisms are important to better understand the

22   processing of such nanoparticles and eventually promote them.

23   In a different context, complex systems containing MoS$_2$ sheets were demonstrated to

24   provoke inflammatory responses eventually exploited to trigger oxidative damages on

25   bacteria or cancer cells towards the development of efficient antibacterial and cancer

26   therapies.[64, 65] Scrolling MoS$_2$ sheets in biomimetic and biological media could be harnessed

27   for future applications. Further studies enquiring on the stability of the nanoscrolls should be

28   conducted to prove that this can constitute a protective mechanism of the structure and be at

29   the source of the inertness of the materials. In addition to intracellular transformation, we also

30   highlighted the role of EV release in resolving the inflammatory environment in the lungs.

31   EVs from BALF of MoS$_2$-exposed mice share most of the EV characteristics in terms of sizes

32   and tetraspanin exposure with the EVs of non-exposed mice, but show more potent protective

33   effect against inflammation, particularly at the early time points after exposure. The secretion

34   of EVs has been proposed as a protective mechanism to prevent autophagy and lysosomal

1 dysfunction. EVs play a major role in disposing of the pathogenic protein load in

2 neurodegenerative disorders such as Alzheimer's and Parkinson's diseases.[33] In addition,

3 EVs can also bind to the extracellularly released pathogenic cargo and facilitate their uptake

4 by phagocytic cells. Although we did not quantify to what extent EVs can shuttle the MoS_2

5 nanosheets or their degradation products and contribute to their propagation or clearance, we

6 have shown that BALF EVs are reshaped by this 2D material to exert anti-inflammatory

7 effects. This can be an alternate pathway to dispose of the nanomaterials and/or restore

8 homeostasis in the lung environment. Our results open also interesting perspectives to better

9 know how the intracellular processing of nanoparticles and the generation of pro-resolving

10 EVs are linked and might participate as defense mechanisms developed by cells to manage

11 different types of nanomaterials. Moreover, future studies need to focus on the EV packaging

12 and specific cargo as function of the (nanoparticle) inflammatory stimulus and decipher their

13 role in the inflammation resolution. Finally, our study serves as a preliminary proof to further

14 consolidate the usage of EVs as a therapeutic option, and would help as first-of-kind study to

15 demonstrate the role of nanoparticle-induced EVs in anti-inflammatory applications.

16

17 **4. Experimental Section**

18 *Synthesis & characterization of 2D MoS_2 nanoparticles.* Layered MoS_2 was obtained through

19 liquid phase exfoliation of bulk MoS_2 crystals in an aqueous solution of bile salts. Bulk MoS_2

20 (400 mg, Sigma-Aldrich) was firstly well mixed with bile salts (200 mg, Sigma-Aldrich) via

21 ball milling (3 h). Exfoliation of MoS_2 was then carried out directly in MilliQ® water (200

22 mL) through bath sonication for 2 h in an ice bath. The resulting dispersion was centrifuged at

23 1500 rpm (402 rcf) for 90 min to remove the bulk MoS_2. The supernatant containing the

24 exfoliated layers of MoS_2 was collected and filtered on a 0.2 µm cut-off membrane. The filter

25 cake was washed with the mixture of water/EtOH (v/v=1:1) for 3 times and MilliQ® water for

26 five times to remove the excess of bile salts. The solid was then sonicated for 10 min in 10

27 mL of MilliQ® water to obtain the final MoS_2 aqueous dispersion at a concentration of 0.15

28 mg/mL. The morphology and the lateral size dimension of 2D MoS_2 were studied by TEM

29 (JEM-2010F, JEOL, Japan). UV-Vis absorption spectrum was recorded on a Cary 5000 UV-

30 Vis-NIR spectrophotometer and was corrected for the baseline and the solvent.

31 Thermogravimetric analyses were performed on a TGA1 (Mettler Toledo) with a ramp of

32 10°C/min under N_2 using a flow rate of 50 mL/min and platinum pans. Zeta-potential

33 measurements were performed on a Beckman Coulter "Delsa Nano Submicron Particle Size

34 and Zeta Potential" instrument, working at ambient conditions. 2D MoS_2 was dispersed at 20

μg/mL in MilliQ® water. Raman spectra were recorded under ambient conditions using a

Renishaw invia spectrometer with a 532 nm laser. The samples were prepared by simply drop

casting the dispersions onto an SiO_2-Si substrate. XPS was performed using Thermo

Scientific KAlpha X-ray spectrometer with a mono X-Ray source Al Kα excitation (1486 eV).

Intratracheal instillation of nanoparticles in mice. In vivo experimental procedures were

approved by the C2EA – 26J Ethics Committee in Animal Experimentation of IRCIV, under

the protocol APAFIS #21089-2019061714166305 v1. Eight-to-ten-week-old healthy male

C57BL/6JRj mice (Janvier Laboratories, Saint-Berthevin, France) were used in this study.

Mice were exposed to MoS_2 nanosheets by intratracheal instillation using a MicroSprayer®

Aerolizer system (MicroSprayer Aerozolizer-Model IA-1C and FMJ-250 High Pressure

Syringe, Penn Century, Wyndmoor, PA). A volume of 50 µL of 5% glucose (vehicle) or with

a suspension containing 1 mg/mL of MoS_2 in 5% glucose was nebulized in each mouse.

The administered dose was based on the work by Wang et al,[66] that assessed lung exposure

in workplaces manufacturing well known NPs. [67,68] Supposing a human exposure of 8 h/day,

5 day per week for 4 months, the authors estimated a total exposure of 92 mg which is

equivalent to 903 µg/m² in the lung. Thus, after transposition to the mouse, we choose a dose

of 2 mg/kg administered by a single intratracheal instillation of a quantity of 50 µg of

NPs/25g mice. This choice is also motivated by the lack of official limit values for these

specific nanomaterial's inhalation exposure observed in human. For the nebulization, mice

were suspended by the upper teeth at a 45° angle, in the supine position, on an intubation

platform (Hallowell EMC, Pittsfield, MA). The mouth was opened, and the tongue was

displaced with the help of a forceps and a mouse intubation speculum (Hallowell EMC)

attached to an otoscope (WelchAllyn Inc., Skaneateles Falls, NY) was inserted for

oropharyngeal visualization. Once a clear view of the trachea was obtained, with the

visualization of the vocal cords, the MicroSprayer tip was endotracheally inserted and 50 µL

of the solution or suspensions were sprayed. The tip was withdrawn and the mouse was taken

off the support and allowed to recover under visual control before being placed back in the

cage. Mice (n=3-8/group) were euthanized at different time points after a single nebulization

(0.5 to 28 days) and the bronchoalveolar lavage fluid was collected.

Bronchoalveolar lavage fluid collection. BALF was collected at different times points (0.5, 1,

2, 7, 14, and 28 days) to analyze cellular and biochemical inflammatory and toxicity markers,

cellular uptake of nanoparticles and EVs. The procedure was performed under anesthesia with

1 a mix of xylazin and ketamin at a final concentration of 1 mg/ml. Briefly, the trachea was

2 surgically exposed and a small incision was made between tracheal rings to allow the

3 insertion of a polyethylene tube attached to a 21G syringe needle, which was secured with a

4 suture thread. Then, the lungs were instilled with saline ice-cold saline solution. The first two

5 lavages (300 and 400 µL) were collected in a 1.5 mL tube and 6 other lavages (700 µL each)

6 in a 15 mL tube, which rendered about 5 mL of BALF. After centrifugation at 500 g for 10

7 min at 4°C, the supernatant from the first two lavages was stored at -20°C for later

8 biochemical analysis, and the cell pellets were pooled and resuspended in 500 µL of saline

9 solution for cell count, using Trypan Blue.

10

11 *Inflammatory cell counts in BALF.* Differential cell count was performed after a cell aliquot

12 from BALF (50 000 cells) was smeared onto slides using Cytospin-4 cytocentrifuge

13 (ThermoFisher Scientific, Saint Aubin, France) at 600 rpm for 10 min, with a break, at room

14 temperature. Cytoslides were stained using the Pappenheim coloration method, with May-

15 Grunwald and Giemsa staining solution (Sigma, Saint-Quentin Fallavier, France), according

16 to the manufacturer's instructions. Then, 400 total cells were manually counted by optical

17 microscopy. Macrophages, neutrophils, eosinophils, basophils, and lymphocytes were

18 identified by their characteristic shapes. Light microscopic images of stained cells were taken

19 with a Leitz Diaplan microscope (Leica Microsystems Wetzlar GmbH, Wetzlar, Germany).

20

21 *Total protein concentration in BALF.* Total protein content in BALF was measured

22 spectrophotometrically at 595 nm according to the Bradford method using bovine serum

23 albumin as standard. The manufacturer's protocol for Bio-Rad Protein Assay (Bio-Rad

24 Laboratories GmbH, Munich, Germany) performed on microtiter plate was followed, and

25 each sample was run in triplicate.

26

27 *Cytokine array assay.* Cell-free BALF of MoS_2 exposed and unexposed mice were processed

28 to assess the levels of various cytokines using the RayBiotech mouse cytokine antibody array

29 C3 (RayBiotech, Tebu-Bio, Le Perray-en-Yvelines, France) according to the manufacturer's

30 instructions. This assay was performed on the BALF pool sample (2-3 BALF from 2-3 mice

31 of the same exposure group were pooled together at (120 µg) final quantity). Briefly, BALF

32 pool samples were added to antibody-coated membranes, and detection of immunoreactive

33 cytokines was performed after sequential incubations of the membranes with biotinylated

34 anti-cytokine antibodies and streptavidin–horseradish peroxidase and visualization by

enhanced chemiluminescence. Images were obtained using a ChemiDoc™Touch Imaging system (Bio-Rad Laboratories). Semiquantitative analysis by densitometry was performed on captured images using Gilles Carpentier's Dot-Blot-Analyzer macro on ImageJ (The macro is available at http://rsb.info.nih.gov/ij/macros/toolsets/Dot%20Blot%20Analyzer.txt). Spots of interest were normalized to an internal positive control after subtraction of representative background sample.

Cell isolation from BALF and transmission electronic microscopy (TEM) characterization.
Cell aliquot from BALF of mice exposed or not to MoS_2 and sacrificed at different time points were seeded onto 6 well plates with complete RPMI medium. After culturing for 12 h, the medium was replaced with fresh RPMI to isolate only the alveolar macrophages (AM) that adhered on the culture flask. For *ex vivo* exposure studies, alveolar macrophages from non-exposed mice were treated with 20 µg/mL MoS_2 for 12 h followed by PBS wash. Then, cells were fixed with 5% glutaraldehyde (Sigma Aldrich, St. Louis, MO, USA) in 0.1 M cacodylate buffer (Sigma Aldrich, St. Louis, MO, USA) for 1 h at room temperature followed by preservation of cells samples in cacodylate buffer. The cells were treated with 1% osmium tetroxide followed by gradient ethanol dehydration. Samples were sectioned and observations were performed using a Hitachi HT7700 microscope (Plateforme Microscopie et Imagerie des micro-organismes, animaux et aliments 2 [MIMA2], UMR1313, INRAE/AgroParis Tech, Jouy-en-Josas, France) operating at 80 kV.

Extracellular vesicle isolation from BALF. EVs from BALF were isolated following a previous protocol.[69] Briefly, BALF isolated from mice of a similar group were pooled to a final volume of 8 mL and centrifuged at 400g for 5 min to remove dead cells and debris. The supernatant was centrifuged at 1500g for 5 min, and the supernatant was filtered using a 0.2 µm syringe filter and stored in ice before isolation. The Amicon Ultra 15 centrifugal filter (100kDa) (Merck, KGaA, Darmstadt, Germany) was equilibrated with PBS at 1500g for 5 min. After discarding the PBS, the filter unit was placed with the BALF sample and centrifuged at 3000g for 30 min, and the BALF EVs were collected and resuspended in 1 mL PBS and stored at -80°C.

BALF EV characterization. EVs isolated were characterized using Nano Tracking Analysis (NTA) instrument (Nanosight NT300, Malvern, UK) for particle concentration determination and size distribution. Samples were diluted with sterile PBS and measurements were made

27

1 once EVs were around 100 events per frame, and averaged based on five videos of 0.5 min

2 each. For TEM observation, EV samples were directly adsorbed onto a carbon film membrane

3 on a 300-mesh copper grid, stained with 1% uranyl acetate, dissolved in distilled water, and

4 dried at room temperature. Grids were examined with a Hitachi HT7700 electron microscope

5 operated at 80kV (Milexia – France), and images were acquired with a charge-coupled device

6 camera (AMT). EV preparations were analyzed by the ExoView® platform (NanoView

7 Biosciences, USA). ExoView® enables the characterization of single EVs captured on a

8 silicon chip layered with an array of antibody spots, anti-CD9 and anti-CD81 for mouse EVs.

9 Interferometric imaging provides size measurements of immobilized particles down to 50 nm,

10 in combination with immunostaining with three fluorescent antibodies targeting

11 transmembrane tetraspanin (anti-CD9, anti-CD63, anti-CD81). All samples were diluted in

12 PBS with 0.05% Tween-20 (PBS-Tw). The samples were incubated on the ExoView

13 Tetraspanin Chip for mouse EVs and placed in a 24-well plate for 16 h at room temperature.

14 The chips were washed 3 times with PBS-Tw. Chips were then fixed and directly incubated

15 with ExoView Tetraspanin Labelling antibodies that consist of anti-CD81 Alexa Fluor®555,

16 anti-CD63 Alexa Fluor®647, and anti-CD9 Alexa Fluor®488. The antibodies were diluted at

17 1:5000 in PBS-Tw with 2% BSA. The chips were incubated with 250 µL of the labeling

18 solution for 2 h, washed in ultrapure water, and dried. The chips were then imaged with the

19 ExoView R100 reader using the ExoScan 2.5.5 acquisition software. The data were analyzed

20 using ExoViewer 2.5.0 with fluorescence thresholds set to detect a maximum of 20 events on

21 the isotype control spots.

22

23 *In vitro differentiation of THP-1 monocytes into macrophages.* We used THP-1 Dual™

24 monocyte cell line (InvivoGen, San Diego, CA, USA), dual reporter cell line which can

25 investigate simultaneous NF-κB signal transduction pathway and IFN pathway via secreted

26 alkaline phosphatase (SEAP) and Lucia luciferase activity, respectively. THP-1 monocytes

27 (InvivoGen, San Diego, CA, USA) were grown with RPMI 1640 (Gibco, Amarillo, TX,

28 USA) supplemented with 10% heat-inactivated fetal bovine serum (FBS), 100 U/mL

29 Penstrep, 100 µg/mL normocin, 10 µg/mL blasticidin, and 100 µg/mL zeocin. Cells were

30 cultured at 37 ºC in humidified cell culture incubator with 5% CO_2. THP-1 macrophages were

31 differentiated from monocytes to using phorbol 12-myristate 13-acetate (PMA) (Sigma, St.

32 Louis, MO, USA). Briefly, 80000 THP-1 monocytes were incubated with 10 ng/mL of PMA

33 for 48 h, where PMA (10 ng/mL) was being replenished after 24 h. After 48 h, THP-1

1 differentiated macrophages were attached to a cell plate and cultured with fresh RPMI media

2 as mentioned above.

3

4 *Investigation of inflammatory pathway in vitro in THP-1 monocytes.* THP-1 monocytes were

5 grown with supplemented with 10 % heat-inactivated fetal bovine serum (FBS), 100 U/mL

6 penstrep, 100 µg/mL normocin, 10 µg/mL blasticidin, and 100 µg/mL zeocin. Cells were

7 cultured at 37 ºC in humidified cell culture incubator with 5% CO_2. Eighty-thousand THP-1

8 monocytes cells were seeded onto a 96-well plate for 24 h and then treated with

9 predetermined concentrations of MoS_2 for 24 h and 72 h. Then, MoS_2 containing medium was

10 removed and cells were rinsed with PBS, followed by centrifugation of 400 g for 5 min. The

11 cells were replenished with complete DMEM media (10 % heat inactivated fetal bovine serum

12 (FBS), 100 U/mL penstrep) for 24 h. The supernatant from the cell plate was utilized for

13 measurement of NFkB and IFN induction. 20 µL of the supernatant was incubated with 180

14 µL of QUANTI-Blue solution per well in a 96 well plate for 3 h at 37 ºC. The NFkB

15 induction was determined by measuring SEAP levels using SpectraMax iD3 multimode plate

16 reader (Molecular Devices, CA, USA) at 655 nm. To measure IFN induction, 10 µL of the

17 sample was incubated with 50 µL of QUANTI-Luc solution per well in a 96 well plate

18 (opaque) and the luminescence was measured using SpectraMax iD3 multimode plate reader

19 (Molecular devices, CA, USA) with an integration time of 400 ms.

20

21 *Alamar Blue assay.* Cell mitochondrial metabolic activity was measured by Alamar Blue

22 assay. THP-1 differentiated macrophages in a 96-well plate were treated with predetermined

23 concentrations of MoS_2 for 24 h. Cells were then washed with fresh PBS followed by

24 incubation with Alamar blue solution (10% v/v) (Thermo Fisher Scientific, MA, USA) in

25 phenol red-free media. After 3-4 h of incubation, the conditioned medium was transferred to a

26 fresh plate for measuring the fluorescence intensity (560/590 nm-excitation/emission).

27 Untreated cells and Triton X (0.3%) served as negative and positive controls respectively.

28 Similarly, Alamar blue assay was performed on THP-1 dual monocytes exposed to different

29 concentrations of MoS_2.

30

31 *In vitro cellular assay for measuring oxidative stress.* A cell-permeable intracellular ROS

32 probe 2'7'-dichlorodihydrofluorescein diacetate (DCFH-DA) (Sigma, St. Louis, MO, USA)

33 that converts to fluorescent DCF in presence of ROS was utilized for the assay. THP-1

34 derived macrophages in a 96-well plate were treated with predetermined concentrations of

1 MoS$_2$ for 4, 24, 48, and 72 h. Then, cells were washed with PBS to remove MoS$_2$ followed by

2 DCFH-DA (100 µM/well) treatment for 40 min in serum-free DMEM media. Then, cells

3 were washed and, replenished with fresh PBS for 30 min incubation in the cell incubator.

4 After 30 min, cells were analyzed for DCF fluorescence (485 nm/ 530 nm-excitation/emission

5 wavelengths). Untreated cells and LPS (100 ng/mL) served as negative and positive controls

6 for oxidative stress respectively.

7

8 *Immunomodulatory effect of BALF EVs on THP-1 dual cells.* The inflammatory status of

9 THP-1 monocytes treated or not with BALF EVs was measured. Eighty-thousand THP-1

10 monocytes were treated with 1×10^9 EVs (particle count measured by NTA) from different

11 BALF groups for 24 h in a 96-well plate. Then the NFκB and IFN induction pathways were

12 quantified as mentioned above. Alternatively, THP-1 monocytes were treated with 1×10^9 EVs

13 for 4 h, followed by EVs wash and replenished with culture media supplemented with LPS

14 (200 ng/ml) for 24 h. The cell supernatant was measured for NFκB and IFN induction

15 pathways were quantified as mentioned above. Untreated cells and LPS (200 ng/mL) served

16 as negative and positive controls.

17

18 *Liquid-cell scanning transmission electron microscopy.* TEM experiments were performed on

19 a double corrected JEOL ARM 200F microscope equipped with a cold field emission electron

20 source and a JEOL 2100F plus microscope with a LaB6 filament source. We used a 200 kV

21 acceleration voltage in both microscopes. For the *in situ* liquid observations, a protochips

22 liquid cell holder (Poseidon Select) was used. The liquid is enclosed at the tip of the holder by

23 two silicon microchips with dimensions of 2×2 mm and 4.5×6 mm, known as bottom and top

24 E-chips respectively. Each E-chip has one 550×50 µm window covered by a 50 nm thick SiN

25 amorphous film. [70, 71] A dispersion of MoS$_2$ nanosheets at 1 mg/mL was sonicated for 15 min

26 before re-dispersing 10 µL in 100 µL of H$_2$O$_2$ 10 mM prepared in DPBS (Dulbecco's

27 phosphate-buffered saline) solution. 1 µL drop of the MoS$_2$-H$_2$O$_2$-DPBS dispersion was

28 placed over the bottom observation window. Immediately after the cell was closed by the top

29 chip and loaded into the microscope. The solution of 10 mM H$_2$O$_2$-DPBS was continuously

30 flushed into the observation chamber at 5 µL/min. After *in situ* experiments the e-chips were

31 recovered, dry out, and analyzed by energy-dispersive X-ray spectroscopy (EDX), high-

32 resolution TEM (HR-TEM), and selected area electron diffraction (SAED).

33

34

Supporting Information

Acknowledgements

References

[1]   K. Kalantar-zadeh, J. Z. Ou, T. Daeneke, M. S. Strano, M. Pumera, S. L. Gras, *Adv. Funct. Mater.* **2015**, *25*, 5086–5099.

[2]   Z. Wang, W. Zhu, Y. Qiu, X. Yi, A. Von dem Bussche, A. Kane, H. Gao, K. Koski, R. Hurt, *Chem. Soc. Rev.* **2016**, *45*, 1750–1780.

[3]   Z. Huang, B. Liu, J.Liu, *Langmuir* **2019**, *35*, 9858–9866.

[4]   S. Karunakaran, S. Pandit, M. De, *ACS Omega* **2018**, *3*, 17532–17539.

[5]   N. Asefifeyzabadi, R. Alkhaldi, A. Z. Qamar, A. A. Pater, M. Patwardhan, K. T. Gagnon, S. Talapatra, M. H. Shamsi, *ACS Appl. Mater. Interfaces* **2020**, *12*, 52156–52165.

[6]   H. Lin, C. Wang, J. Wu, Z. Xu, Y. Huang, C. Zhang, *New J. Chem.* **2015**, *39*, 8492–8497.

[7]   S. Tezuka, T. Seki, T. Ohnishi, H. Noguchi, M. Tanaka, M. Okochi, Y. Hayamizu, *2D Mater.* **2020**, *7*, 024002.

[8]   G. Zeng, T. Chen, L. Huang, M. Liu, R. Jiang, Q. Wan, Y. Dai, Y. Wen, X. Zhang, Y. Wei, *J. Taiw. Inst. Chem. Eng*. **2018**, 205–213.

[9]   X. Zhang, J. Wu, G. R. Williams, S. Niu, Q. Qian, M.-L. Zhu, *Coll. Surf. B, Biointerfaces* **2019**, *173*, 101–108.

[10]   K. Zhang, Y. Zhuang, W. Zhang, Y. Guo, X. Liu, *Drug Deliv.* **2020**, *27*, 909–916.

[11]   V. Yadav, S. Roy, P. Singh, Z. Khan, A. Jaiswal, *Small* **2019**, *15*, 1–33.

[12]   M. K. Jana, C. N. R. Rao, *Philos. Trans. R. Soc. A Math. Phys. Eng. Sci.* **2016**, *374*.

[13]   P. Shah, T. N. Narayanan, C.-Z. Li, S. Alwarappan, *Nanotechnology* **2015**, *26*, 315102.

[14]   J. H. Appel, D. O. Li, J. D. Podlevsky, A. Debnath, A. A. Green, Q. H. Wang, J. Chae, *ACS Biomater. Sci. Eng.* **2016**, *2*, 361–367.

[15]   J. Hao, G. Song, T. Liu, X. Yi, K. Yang, L. Cheng, Z. Liu, *Adv. Sci.* **2017**, *4*, 1600160.

[16]   Z. Wang, A. Von dem Bussche, Y. Qiu, T. M. Valentin, K. Gion, A. B. Kane, R. H. Hurt, *Environ. Sci. Technol.* **2016**, *50*, 7208–7217.

[17]   B. Domi, K. Bhorkar, C. Rumbo, L. Sygellou, S. N. Yannopoulos, R. Quesada, J. A. Tamayo-Ramos, *Nanotechnology* **2020**, *31*.

[18]   M. Cao, R. Cai, L. Zhao, M. Guo, L. Wang, Y. Wang, L. Zhang, X. Wang, H. Yao, C. Xie, Y. Cong, Y. Guan, X. Tao, Y. Wang, S. Xu, Y. Liu, Y. Zhao, C. Chen, *Nat. Nanotechnol.* **2021**, *16*, 708–716.

[19]   R. Kurapati, L. Muzi, A. Perez Ruiz de Garibay, J. Russier, D. Voiry, I. A. Vacchi, M. Chhowalla, A. Bianco, *Adv. Funct. Mater.* **2017**, *27*.

[20] X. Chen, S. M. Shinde, K. P. Dhakal, S. W. Lee, H. Kim, Z. Lee, J. H. Ahn, *NPG Asia Mater.* **2018**, *10*, 810–820.

[21] X. Chen, Y. J. Park, M. Kang, S. K. Kang, J. Koo, S. M. Shinde, J. Shin, S. Jeon, G. Park, Y. Yan, M. R. MacEwan, W. Z. Ray, K. Mi Lee, J. A. Rogers, J. Hyun Ahn, N*at. Commun.* **2018**, *9*, 1–12.

[22] H. Zhao, W. Wu, X. Zhang, Q. Zhu, J. Tang, H. He, G. Chen, J. Qin, *Chemosphere* **2021**, *269*, 128709.

[23] I. Marie, J.-F. Gehanno, M. Bubenheim, A.-B. Duval-Modeste, P. Joly, S. Dominique, P. Bravard, D. Noël, A.-F. Cailleux, J. Benichou, H. Levesque, J-P. Goullé, *Autoimmun. Rev.* **2017**, *16*, 223–230.

[24] G. Filler, V. Belostotsky, M. Kobrzynski, S. H. S. Huang, L. Yang, *Clin. Nephrol.* **2017**, *88*, 79–85.

[25] W. Z. Teo, E. L. K. Chng, Z. Sofer, M. Pumera, *Chem. Eur. J.* **2014**, *20*, 9627–9632.

[26] E. L. K. Chng, Z. Sofer, M. Pumera, *Nanoscale* **2014**, *6*, 14412–14418.

[27] J. Fan, Y. Li, H. N. Nguyen, Y. Yao, D. F. Rodrigues, *Environ. Sci. Nano* **2015**, *2*, 370–379.

[28] C. D. Austin, X. Wen, L. Gazzard, C. Nelson, R. H. Scheller, S. J. Scales, *Proc. Natl. Acad. Sci. U. S. A.* **2005**, *102*, 17987–17992.

[29] N. Luciani, C. Wilhelm, F. Gazeau, *Biomaterials* **2010**, *31*, 7061–7069.

[30] L. W. C. Ho, C. K. W. Chan, R. Han, Y. F. Y. Lau, H. Li, Y. P. Ho, X. Zhuang, C. H. J. Choi, *ACS Nano* **2022**, *16*, 2032–2045.

[31] I. Marangon, N. Boggetto, C. Ménard-Moyon, E. Venturelli, M. L. Béoutis, C. Péchoux, N. Luciani, C. Wilhelm, A. Bianco, F. Gazeau, *Nano Lett.* **2012**, *12*, 4830–4837.

[32] M. Imanbekova, S. Suarasan, T. Rojalin, R. R. Mizenko, S. Hilt, M. Mathur, P. Lepine, M. Nicouleau, N. V. Mohamed, T. M. Durcan, R. P. Carney, J. C. Voss, S. Wachsmann-Hogiu, *Nanoscale Adv.* **2021**, *3*, 4119–4132.

[33] M. Pérez, J. Avila, F. Hernández, *Front. Neurosci.* **2019**, *13*, 1–7.

[34] D. Elgrabli, W. Dachraoui, C. Ménard-Moyon, X. J. Liu, D. Bégin, S. Bégin-Colin, A. Bianco, F. Gazeau, A. Alloyeau, *ACS Nano* **2015**, *9*, 10113–10124.

[35] A. Balfourier, N. Luciani, G. Wang, G. Lelong, O. Ersen, A. Khelfa, D. Alloyeau, F. Gazeau, F. Carn, *Proc. Natl. Acad. Sci. U. S. A.* **2020**, *117*, 103–113.

[36] A. K. Andriola Silva, C. Wilhelm, J. Kolosnjaj-Tabi, N. Luciani, F. Gazeau, *Pharm. Res.* **2012**, *29*, 1392–1403.

[37] M. Eldh, K. Ekström, H. Valadi, M. Sjöstrand, B. Olsson, M. Jernås, J. Lötvall, *PLoS*

One **2010**, *5*, 1–8.

[38]   M. Saeed-Zidane, L. Linden, D. Salilew-Wondim, E. Held, C. Neuhoff, E. Tholen, M.

Hoelker, K. Schellander, D. Tesfaye, *PLoS One* **2017**, *12*, 1–24.

[39]   D. K. Ji, Y. Zhang, Y. Zang, J. Li, G. R. Chen, X. P. He, H. Tian, *Adv. Mater.* **2016**,

28, 9356–9363.

[40]   C. N. Serhan, S. D. Brain, C. D. Buckley, D. W. Gilroy, C. Haslett, L. A. J. O'Neill,

M. Perretti, A. G. Rossi, J. L. Wallace, *FASEB J.* **2007**, *21*, 325–332.

[41]   C. T. Robb, K. H. Regan, D. A. Dorward, A. G. Rossi, *Semin. Immunopathol.* **2016**,

38, 425–448.

[42]   C. Busch, J. Favret, L. Geirsdóttir, K. Molawi, M. Sieweke, *Bio-Protocol* **2019**, *9*, 1–

13.

[43]   E. A. Veal, A. M. Day, B. A. Morgan, *Mol. Cell* **2007**, *26*, 1–14.

[44]   C. Lennicke, J. Rahn, R. Lichtenfels, L. A. Wessjohann, B. Seliger, *Cell Commun.*

Signal. **2015**, *13*, 1–19.

[45]   S. H. Song, B. H. Kim, D. H. Choe, J. Kim, D. C. Kim, D. J. Lee, J. M. Kim, K. J.

Chang, S. Jeon, *Adv. Mater.* **2015**, *27*, 3152–3158.

[46]   E. Ji, J. Son, J. H. Kim, G. H. Lee, *FlatChem* **2018**, *7*, 26–33.

[47]   X. Cui, Z. Kong, E. Gao, D. Huang, Y. Hao, H. Shen, C. A. Di, Z. Xu, J. Zheng, D.

Zhu, *Nat. Commun.* **2018**, *9*, 1–7.

[48]   J. Meng, G. Wang, X. Li, X. Lu, J. Zhang, H. Yu, W. Chen, L. Du, M. Liao, J. Zhao,

P. Chen, J. Zhu, X. Bai, D. Shi, G. Zhang, *Small* **2016**, 3770–3774.

[49]   P. Cao, J. Wu, *Langmuir* **2021**, *37*, 4971–4983.

[50]   Z. Wang, H. H. Wu, Q. Li, F. Besenbacher, X. C. Zeng, M. Dong, M. *Nanoscale* **2018**,

10, 18178–18185.

[51]   C. Y. Xu, J. K. Qin, H. Yan, Y. Li, W. Z. Shao, L. Zhen, *Appl. Surf. Sci*. 2018, 451–

456.

[52]   S. L. Xiao, W. Z. Yu, S. P. Gao, *Surf. Sci.* **2016**, *653*, 107–112.

[53]   B. Munkhbat, A. B. Yankovich, D. G. Baranov, R. Verre, E. Olsson, T. O. Shegai,

Nat. Commun. **2020**, *11*, 4604.

[54]   T. G. Novak, J. Kim, A. P. Tiwari, J. Kim, S. Lee, J. Lee, S. Jeon, *ACS Sustain. Chem.*

Eng. **2020**, *8*, 11276–11282.

[55]   X. S. Chu, D. O. Li, A. A. Green, Q. H. Wang, *J. Mater. Chem. C* **2017**, *5*, 11301–

11309.

[56]   V. Ruiz, E. Meux, M. Schneider, V. Georgeaud, *Ind. Eng. Chem. Res.* **2011**, *50*, 9,

5307–5315.

[57]   L. Dong, S. Lin, L. Yang, J. Zhang, C. Yang, D. Yang, H. Lu, *Chem. Commun.* **2014**, *50*, 15936–15939.

[58]   E. L. Khim Chng, C. K. Chua, M. Pumera, *Nanoscale* **2014**, *6*, 10792–10797.

[59]   S. Qiang, Z. Li, L. Zhang, D. Luo, R. Geng, X. Zeng, J. Liang, P. Li, Q. Fan, *Nanomaterials* **2021**, *11*, 1–12.

[60]   A. M. Dimiev, A. Khannanov, I. Vakhitov, A. Kiiamov, K. Shukhina, J. M. Tour, *ACS Nano* **2018**, *12*, 3985–3993.

[61]   L. Pastor, E. Vera, J. M. Marin, D. Sanz-Rubio, *Int. J. Mol. Sci.* **2021**, *22*, 1–21.

[62]   X. Zhu, X. Ji, N. Kong, Y. Chen, M. Mahmoudi, X. Xu, L. Ding, W. Tao, T. Cai, Y. Li, T. Gan, A. Barrett, Z. Bharwani, H. Chen, O. C. Farokhzad, *ACS Nano* **2018**, *12*, 2922–2938.

[63]   C. Moore, A. Harvey, J. N. Coleman, H. J. Byrne, J. McIntyre, *2D Mater.* **2020**, *7*, 025003.

[64]   Y. Sang, W. Li, H. Liu, L. Zhang, H. Wang, Z. Liu, J. Ren, X. Qu, *Adv. Funct. Mater.* **2019**, *29*, 1900518.

[65]   Y. Wei, S. Wu, Z. Liu, J. Niu, Y. Zhou, J. Ren, X. Qu, *Materials Today* **2022**, *56*, 16-28.

[66]   X. Wang, N. D. Mansukhani, L. M. Guiney, Z. Ji, C. H. Chang, M. Wang, Y. P. Liao, T. Song, B. Sun, R. Li, T. Xia, M. C. Hersam, A. E. Nel, *Small* **2015**, *11*, 5079–5087.

[67]   J. H. Lee, M. Kwon, J. H. Ji, C. S. Kang, K. H. Ahn, J. H. Han, I. J. Yu, *Inhal. Toxicol.* **2011**, *23*, 226–236.

[68]   J. M. Antonini, M. A. Badding, T. G. Meighan, M. Keane, S. S. Leonard, J. R. Roberts, *Environ. Health Insights* **2014**, *8*, 11–20.

[69]   T. Parimon, N. E. Garrett, P. Chen, T. J. Antes, *J. Vis. Exp.* **2018**, *2018*, 1–9.

[70]   A. Khelfa, J. Nelayah, H. Amara, G. Wang, C. Ricolleau, D. Alloyeau, D. *Adv. Mater.* **2021**, *33*, 1–9.

[71]   A. Khelfa, J. Nelayah, G. Wang, C. Ricolleau, D. Alloyeau, *J. Vis. Exp.* **2021**, *2021*, 1–17.

MoS_2 nanosheets trigger lung inflammation that is fast recovered although the products derived from their degradation remain in the alveolar macrophages and in the extracellular vesicles up to 30 days. MoS_2 is *in vivo* biotransformation is caused by reactive oxygen species following three mechanisms: scrolling, etching and oxidation, generating molybdate ions and oxide nanoparticles.

Nathaly Ortiz Peña, Kondareddy Cherukula, Benjamin Even, Ding-Kun Ji, Sarah Razafindrakoto, Shiyuan Peng, Amanda K. A. Silva, Cécilia Ménard Moyon, Hervé Hillaireau, Alberto Bianco,* Elias Fattal,* Damien Alloyeau,* Florence Gazeau*

Resolution of MoS_2 nanosheets-induced pulmonary inflammation driven by nanoscale intracellular transformation and extracellular-vesicle shuttles
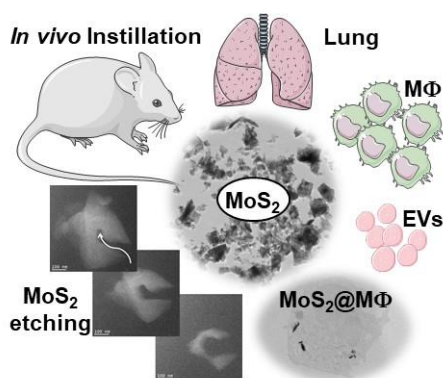
Supporting Information

Resolution of MoS₂ nanosheets-induced pulmonary inflammation driven by nanoscale intracellular transformation and extracellular-vesicle shuttles

Nathaly Ortiz Peña, Kondareddy Cherukula, Benjamin Even, Ding-Kun Ji, Sarah Razafindrakoto, Shiyuan Peng, Amanda K. A. Silva, Cécilia Ménard Moyon, Hervé Hillaireau, Alberto Bianco,* Elias Fattal,* Damien Alloyeau,* Florence Gazeau*
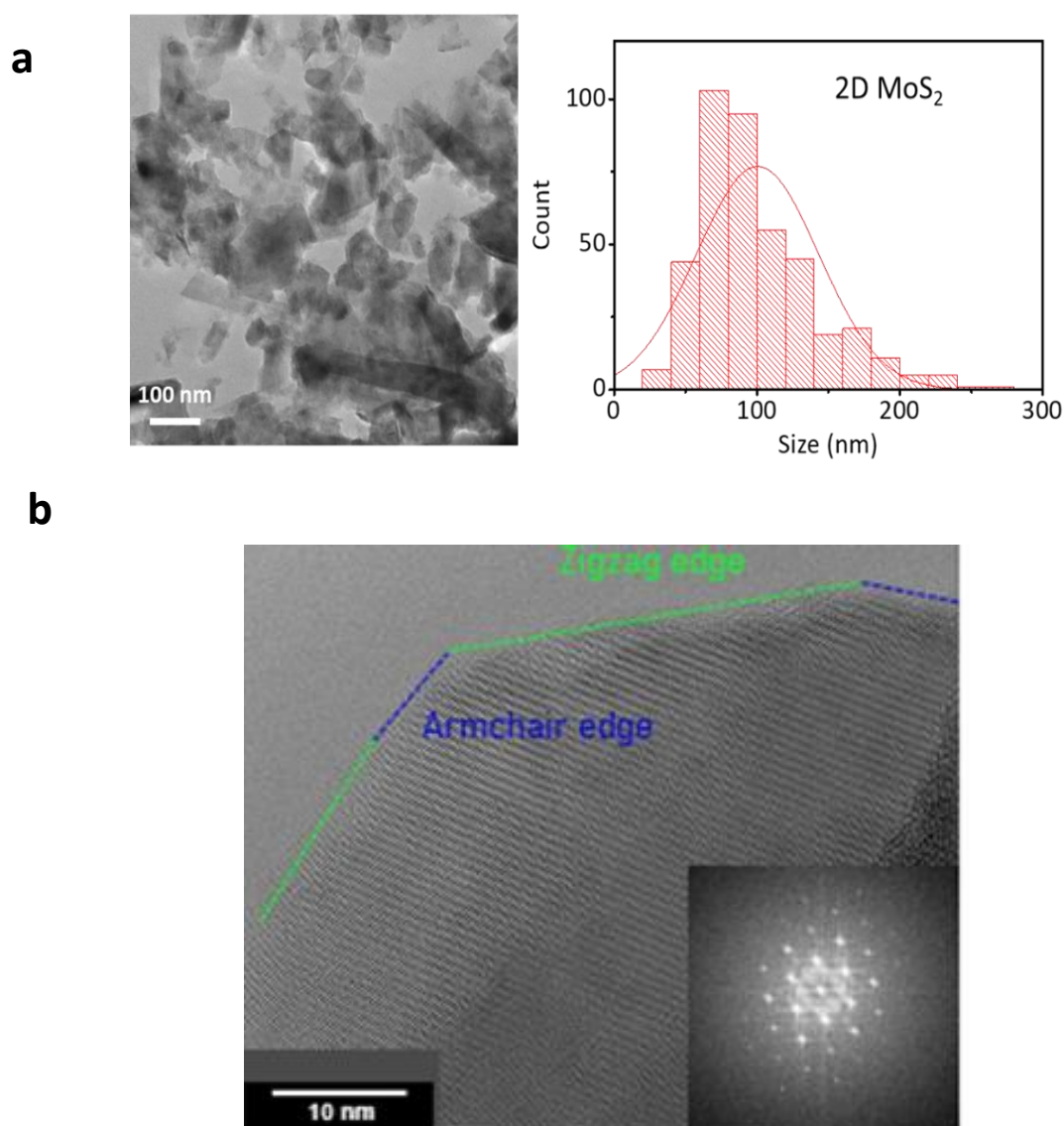
Figure S1. (a) TEM images and lateral size dimension of 2D MoS₂ nanosheets. **(b)** HR-TEM structure of a MoS₂ sheet showing armchair and zigzag edges and corresponding fast Fourier transform in inset.
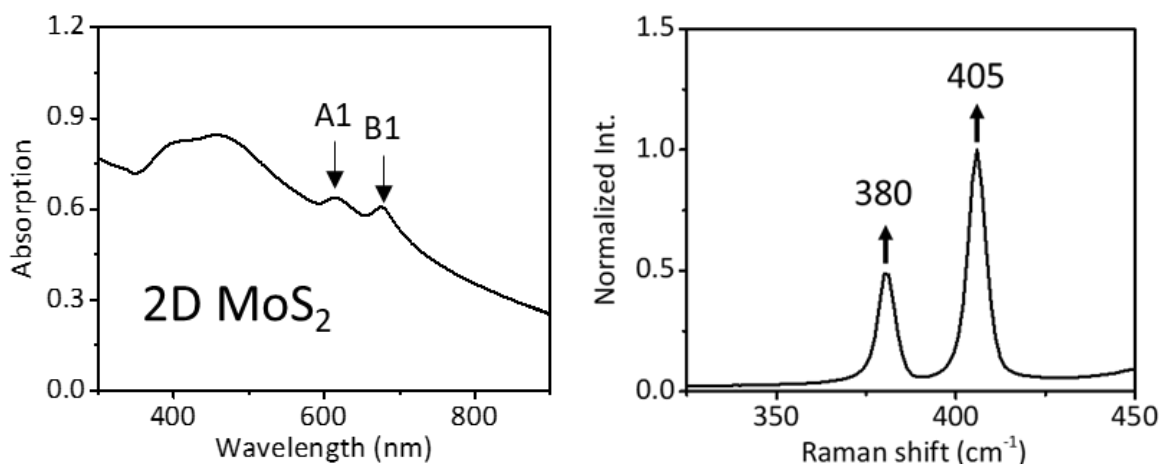
Figure S2. UV-Vis and Raman spectra of 2D MoS_2 nanosheets. Absorbance peaks at 610 and 670 nm are ascribed to the A1 and B1 direct exciton transitions of 2D MoS_2 nanosheets with energy split from the spin–orbital coupling of energy band, respectively (left). The two bands at 405 and 380 cm^{-1} are characteristics of the A_{1g} (out-of-plane vibration of S) and E^1_{2g} (in-plane relative motion between S and Mo) modes of the hexagonal MoS_2 crystal (right).
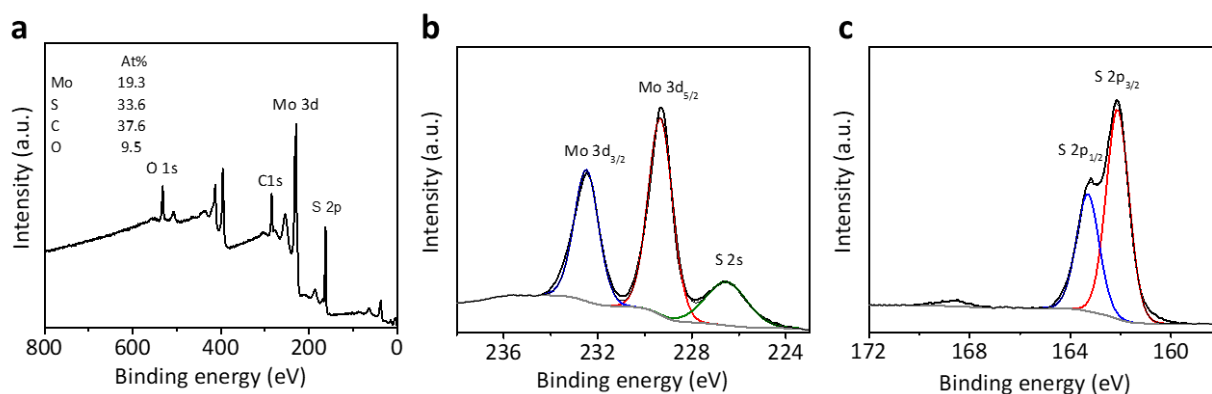

Figure S3. XPS survey (a) and high-resolution Mo 3d (b) and S 2p (c) spectra of MoS_2.
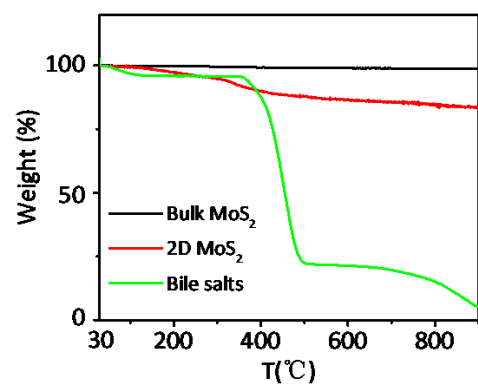
Figure S4. TGA of 2D MoS₂ nanosheets. The weight loss of 2D MoS₂ nanosheets at 600°C is 13%, corresponding to an amount of bile salts of 325 μmol/g.
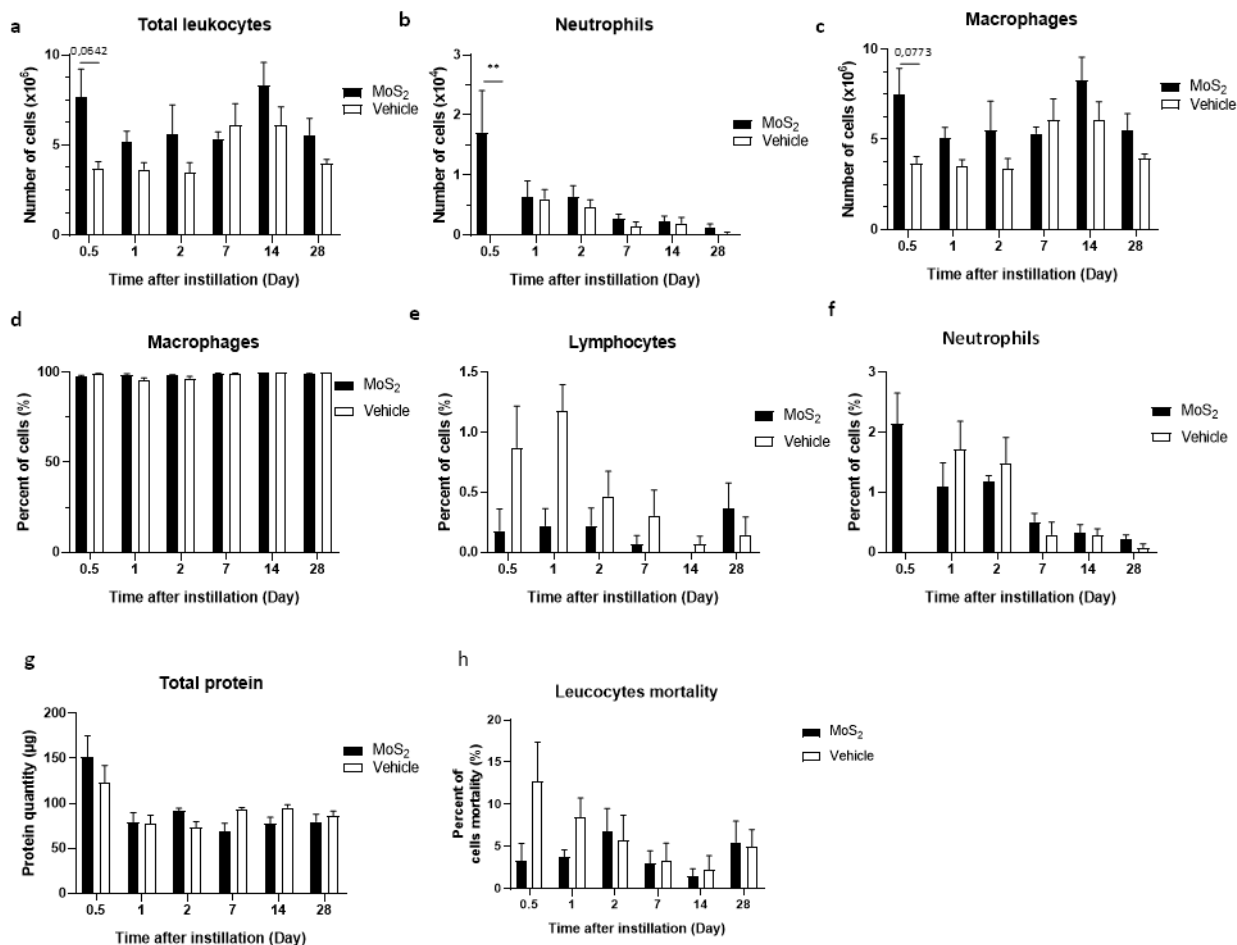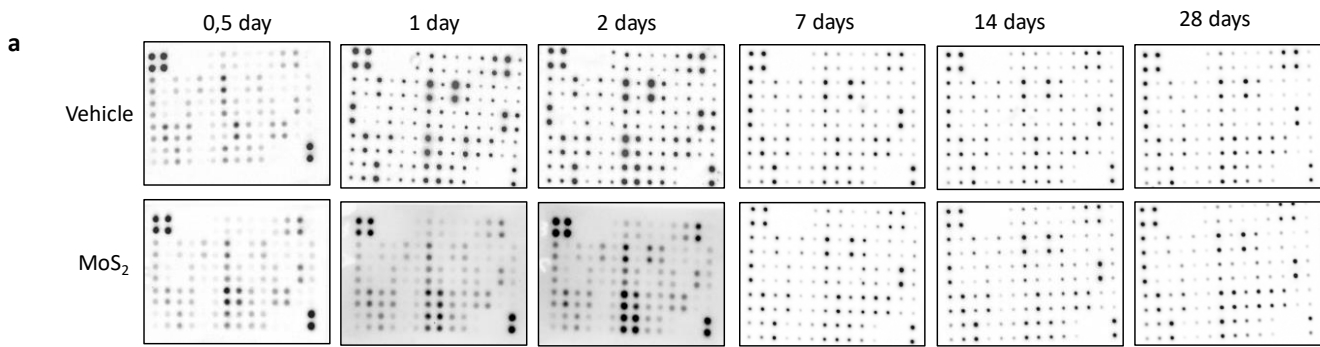
Figure S5. Analysis of cells and proteins recovered from BALF of MoS_2-exposed or vehicle-exposed mice. Number of mice: n=3 (0.5 day); n=4 (1, 2, 7, 14 and 28 days). Statistical significance was calculated using one-way ANOVA (Bonferonni's multiple comparisons test). Quantification of total leukocytes (a), macrophages (b) and neutrophils (b) recovered from BALF of MoS_2-exposed or non-exposed (vehicle) mice at different time-points after instillation. Percentage in total BALF cells of macrophages (d), neutrophils (e) and, lymphocytes (f). (g) Protein quantification in BALF. (h) Leukocytes mortality.

		A	B	C	D	E	F	G	H	I	J	K	L	M	N
Each antibody is spotted in duplicate vertically	1	POS	POS	NEG	NEG	BLANK	Axl	BLC (CXCL13)	CD30 Ligand (TNFSF8)	CD30 (TNFRSF8)	CD40 (TNFRSF5)	CRG–2	CTACK (CCL27	CXCL16	Eotaxin-1 (CCL11)
	2														
	3	Eotaxin-2 (CCL24)	Fas Ligand (TNFSF6)	Fractalkine (CX3CL1)	GCSF	GM-CSF	IFN-gamma	IGFBP-3	IGFBP-5	IGFBP-6	IL-1 alpha (IL-1 F1)	IL-1 beta (IL-1 F2)	IL-2	IL-3	IL-3 R beta
	4														
	5	IL-4	IL-5	IL-6	IL-9	IL-10	IL-12 p40/p70	IL-12 p70	IL-13	IL-17A	KC (CXCL1)	Leptin R	Leptin	LIX	L-Selectin (CD62L)
	6														
	7	Ltn (XCL1)	MCP-1 (CCL2)	MCP-5	M-CSF	MIG (CXCL9)	MIP-1 alpha (CCL3)	MIP-1 gamma	MIP-2	MIP-3 beta (CCL19)	MIP-3 alpha (CCL20)	PF-4 (CXCL4)	P-Selectin	RANTES (CCL5)	SCF
	8														
	9	SDF-1 alpha	TARC (CCL17)	I-309 (TCA-3/CCL1)	TECK (CCL25)	TIMP-1	TNFalpha	TNF RI (TNFRSF1A)	TNF RII (TNFRSF1B)	TPO	VCAM-1 (CD106)	VEGF-A	BLANK	BLANK	POS
	10														

Figure S6. Detection of 62 cytokines in BALF of mice exposed to MoS_2 or vehicle at different time points after exposure. (a) Representative image of cytokine array for each conditions. (b) Array map RayBio® C-Series Mouse Cytokine Antibody Array C3.
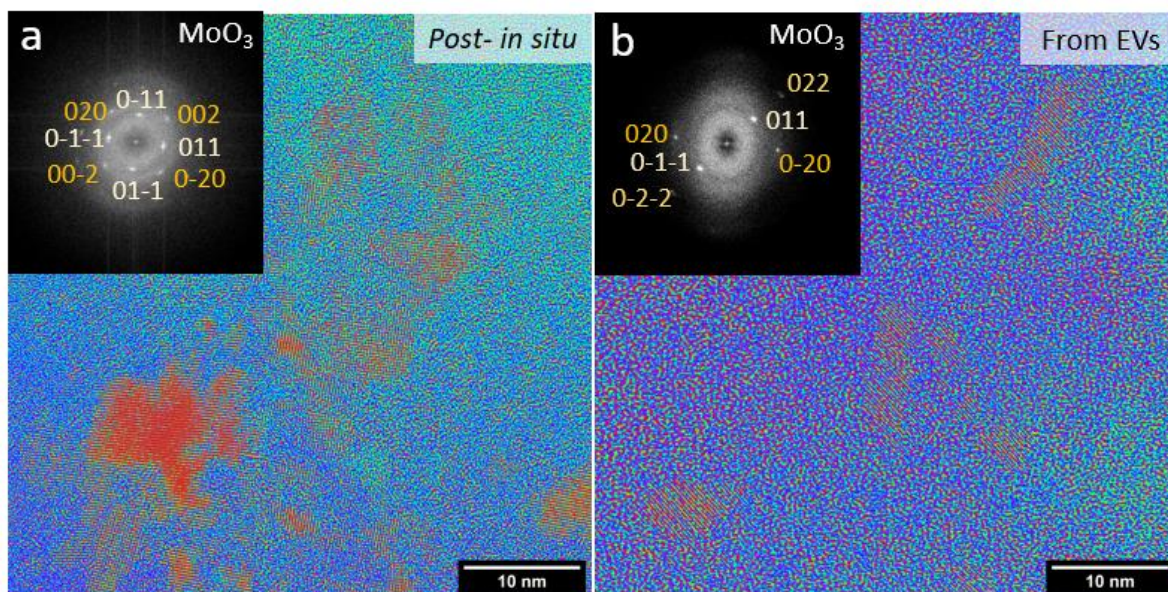
Figure S7. (a) HR-TEM of *post-in situ* fragments of the patches displaying oxidation. Inset FFT of the fragments displaying the diffraction patterns of MoO_3. (b) Fragments showing MoO_3 structure found within extracellular vesicles recovered from ex vivo alveolar macrophages 24 h post-exposure to MoS_2.
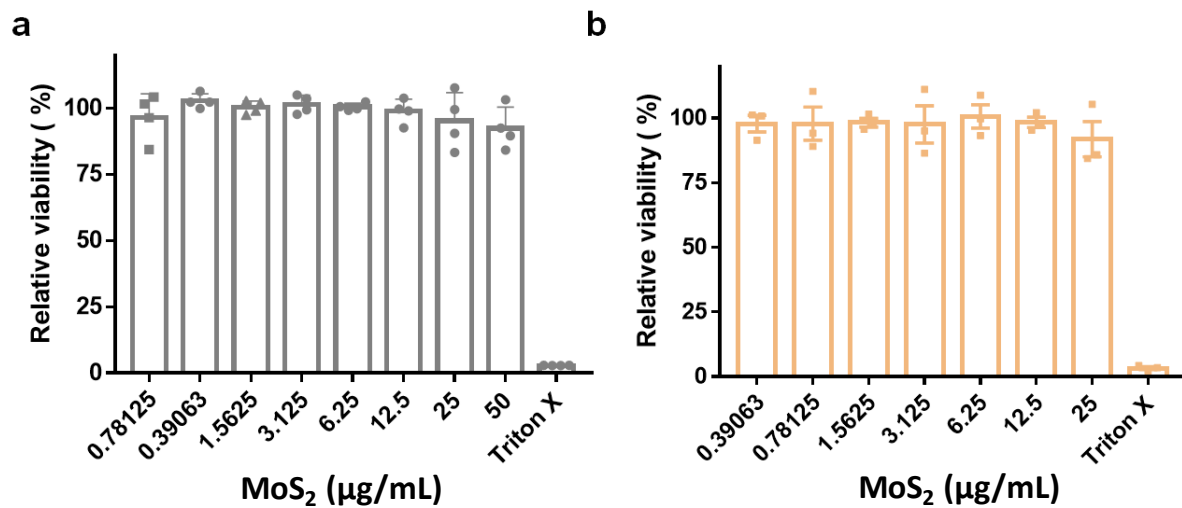
Figure S8. Alamar Blue assay depicting the mitochondrial activity (relative viability compare to non-exposed cells) of THP-1 macrophages. (b) Relative viability of THP-1 Dual monocytes after exposure to MoS_2 at different concentrations in complete medium for 24 h.
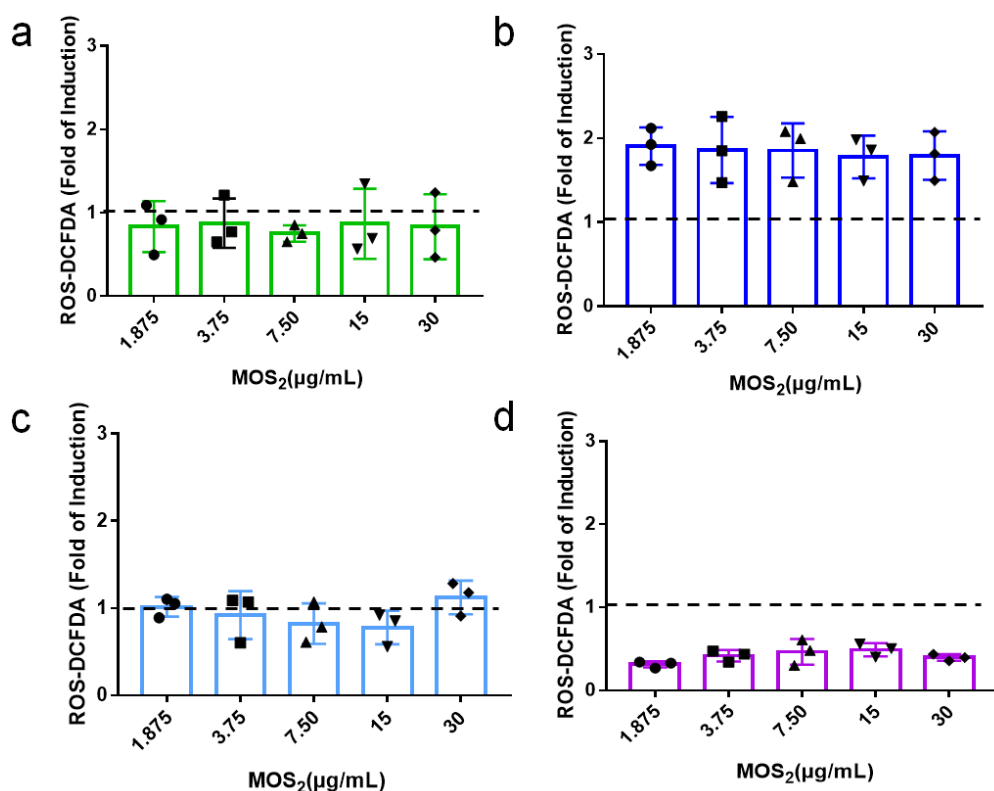
Figure S9. Oxidative stress measured after (a) 4 h (b) 24 h (c) 48 h (d) 72 h incubation of MoS_2 at different concentrations with THP-1 macrophages.

Supporting Movies

Movie 1. *In situ* liquid phase STEM recording of MoS_2 sheets in 10 mM H_2O_2-DPBS. Initial stacked MoS_2 sheets started to further disperse and subsequently folded and scrolled as highlighted in Figure 4a. The video has been accelerated from 3fps to 100 fps.

Movie 2. *In situ* liquid phase STEM recording of free-standing MoS_2 patch scrolling in 5 mM H_2O_2-DPBS. The video has been accelerated from 3fps to 100 fps.

Movie 3. *In situ* liquid phase STEM recording of MoS_2 scroll in 5 mM H_2O_2-DPBS unfolding. This observation points how the scrolling seems to be highly dynamic and reversible. The video has been accelerated from 3fps to 100 fps.

Movie 4. *In situ* liquid STEM etching of MoS_2 patches in 5 mM DPBS-H_2O_2 solution. The video has been accelerated from 3fps to 100 fps.

Movie 5. *In situ* liquid STEM displaying internal etching from edge defects of a single MoS_2 sheet in 5 mM DPBS-H_2O_2 solution. The video has been accelerated from 3fps to 100 fps.